SPIN POLARIZED TUNNELING IN HYBRID MAGNETIC TUNNEL JUNCTIONS COMPRISING C_{60}

Thesis for graduation as Master of Science in Nanotechnology

by

Quyen T. Le

Supervised by

Assistant Prof. Dr. Michel de Jong

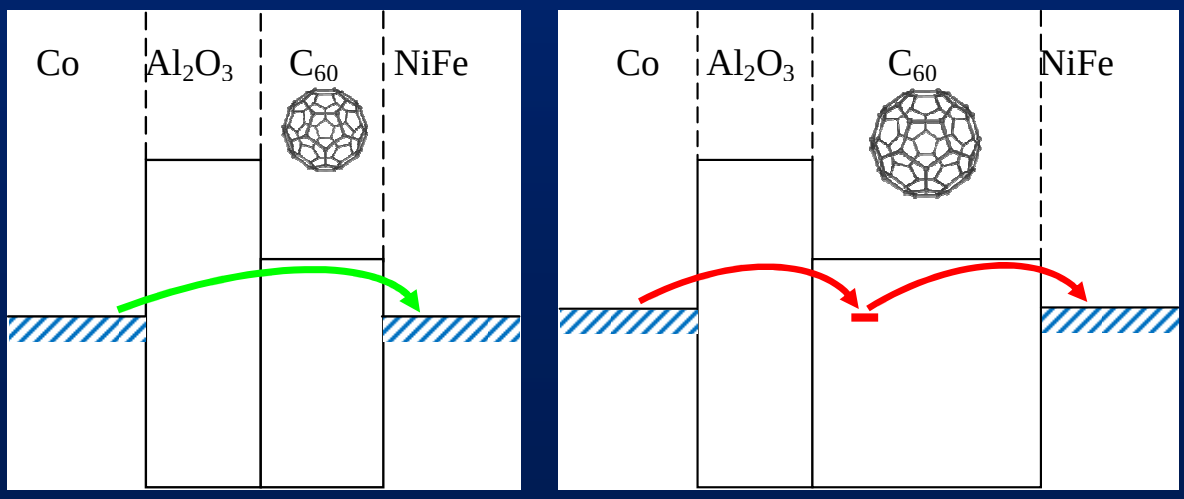

University of Twente

July 2011

SPIN POLARIZED TUNNELING

IN HYBRID MAGNETIC TUNNEL JUNCTIONS

COMPRISING C_{60}

by

Quyen T. Le

A Thesis Submitted in
Partial Fulfillment of the
Requirements for the Degree of

Master of Science
in Nanotechnology

at
University of Twente
July 2011

Approved:
Prof. Dr. Wilfred van der Wiel
Assistant Prof. Dr. Michel de Jong
Prof. Dr. Paul Kelly
Ir. Lan Anh Tran

ABSTRACT

Organic semiconductor spintronics has been extensively studied over the past decade due to the expectation of the exceptionally long spin lifetimes in carbon-based semiconductors. This prospective characteristic raises the hope for organic semiconductors as potential materials for developing spintronic applications such as spin based quantum computing and spin based organic light emitting diodes. Although spin transport in organic semiconductors is fascinating and potentially very useful, there are many challenges, both in understanding fundamental properties and, at a later stage, in obtaining high-quality devices.

In this master project, carbon-based molecules (C_{60}) were inserted into Co/Al_2O_3/NiFe magnetic tunnel junction structures to form vertical spin transport devices. By varying the C_{60} thickness from 0 to 20 nm, the vertical device geometry allows for the investigation of different spin-dependent transport regimes. Our results provide strong evidence of spin polarized tunneling as the dominant transport mechanism in C_{60}-based magnetic tunnel junctions. Furthermore, based on the distinctive performance of devices with different C_{60} thickness, we can also identify between direct and two-step tunneling in junctions with 0–7 nm C_{60}. This work presents the understanding of spin polarized transport in vertical organic spin transport devices. Moreover, we propose several approaches for further study to circumvent the conductivity mismatch problem and improve the efficiency of C_{60}-based spin transport devices.

ACKNOWLEDGEMENT

This study is part of the Master (MSc) program in Nanotechnology at the University of Twente. I have been awarded University of Twente Scholarship (UTS) to follow this MSc program for two years. This Master's thesis is the result of a research project in the Nano-Electronics (NE) Group led by Prof. Dr. Wilfred van der Wiel at the MESA+ Institute for Nanotechnology in University of Twente.

Foremost, I would like to thank Wilfred and Michel for giving me an opportunity to join NE group and work under their guidance. Being part of this ambitious and joyful group, I have not only gained invaluable scientific experiences but also had a warm feeling of being in a family. To Michel, I am definitely indebted for his very sharp advices and quick help at any time needed. I sincerely admire Michel for his knowledge and passion for science as well as share my respect for the way he cares for his family. This convinces me that a scientist has enough time for his/her family and inspires me to go further in the challenging scientific career ahead.

I am grateful to Lan Anh, my daily supervisor, for her infinite help and advices in work and in life. To me, she is not only a supervisor but also a friend and a sister. I highly appreciate Johnny, Thijs and Martin for troubleshooting many difficulties for me when working with DCA, Bruker and AFM. I am also thankful to Tian for his advices on both theoretical and experimental aspects in my study. I have learned a lot during doing experiments and working together with them.

Furthermore, I would like to thank everybody with whom I have shared experiences in life since the first day I came to the Netherlands. I very much enjoyed the funny jokes of Michel Z. and Koert during lunches, Friday night movies/experiments with Maarten and Janine, talking

with Peter and Bernardus. I am very happy because I have had you guys to share the joys and difficulties in my life. Many thanks for the Vietnamese community in University of Twente for always being a family for me and helping me during the time I lived abroad.

Last but not least, I am grateful to my family and my boyfriend for their unconditional love and support. Grandparents, Mum, Uncle, brother, cousins and my honey, your loves are my strongest motivation and belief.

CONTENTS

CHAPTER 1

INTRODUCTION

1. Spintronics

Spintronics (spin-electronics) investigates control and manipulation of the electron spin in metals and semiconductors. There were already research activities on- and commercial applications of spin effects before the advent of spintronics, such as the anisotropic magneto-resistance (AMR) effect which was used in the magnetic read heads of previous generations of hard disks. However, along with the development of nanotechnology, it has become possible to fabricate nanostructures in which a spin polarization of the current adds more prospective new functionalities to devices.

Since the discovery of the giant magnetoresistance (GMR) effect in 1988, for which the Nobel Prize in Physics 2007 was awarded to Peter Grünberg and Albert Fert, spintronics has received a great deal of interest. The discovery of GMR is considered as a starting point for the field of spintronics, which deals with understanding the physics of the interaction between spins and, for example, charges as well as spin polarized tunneling, and building applications based on these phenomena. GMR's most well known application is the Hard Disk Driver (HDD). Besides, applications of GMR are as diverse as automotive sensors, solid-state compasses and non-volatile magnetic memories.

Recently, the large tunneling magnetoresistance (TMR) observed in magnetic tunnel junctions (MTJs) due to spin-polarized tunneling has garnered much attention. This has already been pioneered by Julliere in the mid 70s [1] but did not develop strongly due to the technological difficulties at that time. However, until the mid 90s, along with the advent of

superior fabrication techniques, when TMR effects of about 10% were proven to exist at room temperature [2, 3], the hope has been raising that TMR effects might be used as widely as GMR effects, with the advantage of providing higher magnetoresistive signal amplitudes. In fact, the current-perpendicular-to-plane (CPP) TMR read head was commercialized in 2005 and has replaced the current-in-plane (CIP) GMR read head. It is expected that CPP-GMR sensors will again replace the TMR sensors in HDDs, because CPP-GMR sensors enable much higher areal densities.

Nowadays spintronics research focuses more and more on harnessing spins in semiconductors, with the prospect of developing devices with new or improved functions. In this respect, spin transport in *organic* semiconductors (OSCs) is potentially useful due to the expectation of exceptionally long spin lifetimes in these materials. Organic materials have relatively weak spin-orbit interaction and weak hyperfine interaction, both of which contribute to randomizing the spins, so that spin memory in organic materials is expected to be as long as a few seconds [4, 5]. Such features make OSCs ideal for realizing devices in which a large amount of spin operations are required.

2. Progress in organic spintronics

In the past decade, observations of magnetoresistance (MR) effects in OSCs have opened up the potential of these materials for spin-conserving transport. Significant progress has been made in the effort to understand the underlying physics involved in spin injection, detection and transport in OSCs as well as the anomalous magnetoresistance of these materials, although many open questions remain as well. Effective spin injection and detection is a prerequisite for the application of organic materials as spin transport media for spin electronics applications. Up to

date, most research in this direction has focused on tris(8-hydroxyquinolinato) aluminum (Alq_3), a small-molecule (as opposed to polymer) organic semiconductor that is widely used as electron transporting and light-emitting material in organic light-emitting diodes (OLEDs).

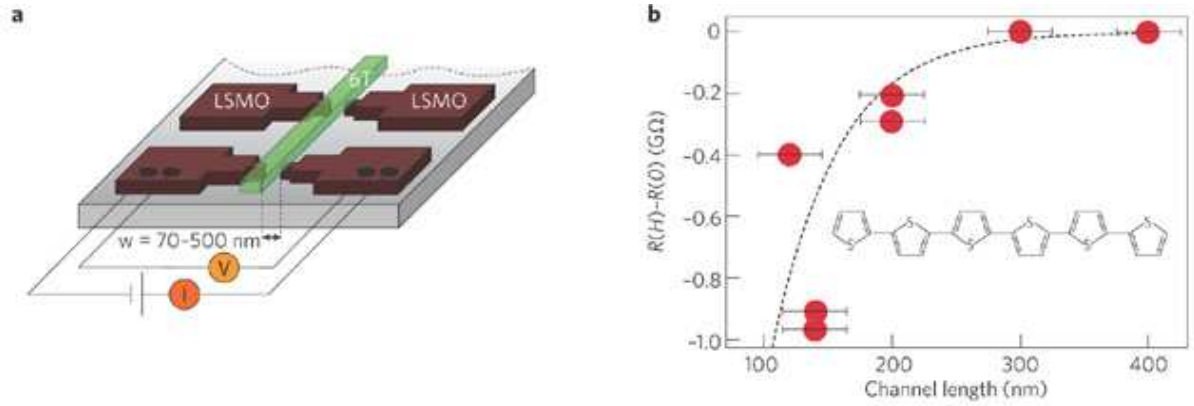

Figure 1.1: (a) Schematic view of hybrid junction and dc four-probe electrical scheme and (b) Magnetoresistance (H = 0.3 T, where H is the magnetic field) of the lateral spin device depicted in (a) as a function of the channel length (from reference [6], reproduced in reference [5]).

In 2002, Dediu *et al.* measured the change in resistance of sexithiophene (T_6) thin films deposited onto two $La_{0.67}Sr_{0.33}MnO_3$ (LSMO) electrodes separated by a narrow channel defined by e-beam lithography [6]. Channel lengths ranged from 70 to 500 nm thick with 100-nm-thick LSMO films and 100 to 150-nm-thick T_6 films (Figure 1.1a). In this research, the highest resistance change was 30% by applying a 3.4 kOe magnetic field, which was obtained for a 140-nm-long channel. However, the resistance change observed in this work could not be straightforwardly attributed to the conventional spin-valve effect because the relative magnetization orientation of two LSMO electrodes could not be set to an antiparallel configuration. Instead, a random- versus parallel magnetization alignment was used, by applying a strong out-of-plane magnetic field.

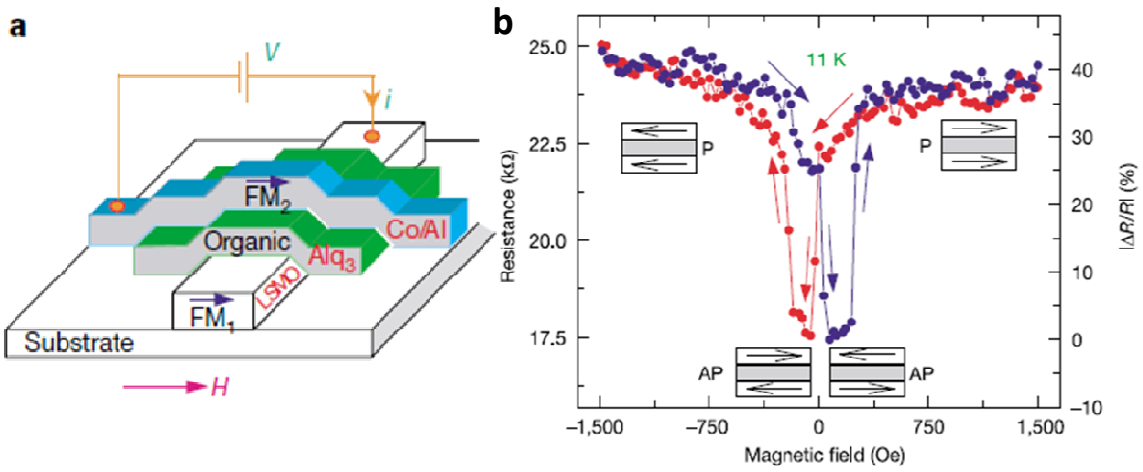

Figure 1.2: (a) Schematic structure of device with OSC spacer and (b) GMR loop of a LSMO (100 nm)/Alq_3 (130 nm)/Co (3.5 nm) spin-valve device measured at 11 K in reference [7].

In 2004, Xiong *et al.* reported the first observation of spin transport through a "thick" (on the order of 100 nm) layer of Alq_3 using a vertical spin valve structure [7]. In this study, a device with structure LSMO/Alq_3/Co was formed by depositing Alq_3 onto LSMO followed by a thin Co layer. The thickness range of Alq_3 (d) used ranged from 130 to 260 nm. The authors estimated a spin diffusion length of 45 nm. Their device with a 130 nm thick layer of Alq_3 exhibited an inverse GMR of about 40% at 11 K (Figure 1.2b). When the Alq_3 film thickness was increased or the sample temperature was increased, the MR dropped rapidly and reduced to zero when T >200 K. Based on the analysis and comparison of the *IV* responses between devices with $d < 100\,nm$ and $d > 100\,nm$, the authors indicated a dual conduction regime between coherent tunneling and incoherent hopping in devices with $d > 100\,nm$.. Following this initial report, lots of studies focusing on spin transport in Alq_3 have been carried out by different groups. Although there have been many observations of the negative MR in LSMO/Alq_3/Co devices, the uncertainty about the exact details of the transport mechanism still remains.

In addition to the studies discussed above, experiments that can be unambiguously attributed to direct tunneling transport of spin-polarized charge carriers in magnetic tunnel junctions based on Alq_3 [8, 9] have been reported. In 2007, Santos *et al.* observed room temperature MR of magnetic tunnel junctions with hybrid Al_2O_3/Alq_3 and Alq_3 tunnel barriers. For both junction structures, they observed positive MR in contrast to the inverse MR in reference 7. The authors indicated that the inverse GMR in reference 7 may originate from the opposite spin asymmetry coefficients of Co and LSMO. Meanwhile, in their work, the positive sign of the TMR is consistent with the known spin polarization of Co and NiFe thin films. Additionally, MTJs with up to 20-nm-thick Alq_3 films grown directly on the Co layer were unstable and did not show proper tunneling characteristics, which indicated multistep conduction via gap states at the Co/Alq_3 interface. Presently, Barraud *et al.* observed a TMR as large as 300% at 2 K in a $La_{0.7}Sr_{0.3}MnO_3/Alq_3/Co$ tunnel junction, however the TMR vanished below the noise level at 180 K [9]. A new spin injection mechanism was proposed to explain both the positive MR of devices with thin Alq_3 tunnel barriers [8, 9] and negative MR observed for larger and thicker Alq_3 barriers in the Xiong *et al*. publication [7]. In this model, the effective spin polarization of the electrodes can be change dramatically due to the formation of spin-hybridization-induced polarized states in the first monolayer at the electrode interface, which emphasizes the role of the interface between ferromagnet and the tunnel barrier. Overall, although the origin of effects of interface on tunnel spin polarization is still under debate, it is clear that the hybridization of states at the interface plays an important role.

Although there has been a lot of promising results obtained, there are still many remaining questions in this area. The spin relaxation mechanisms in organic materials are still an incompletely answered question. The processes responsible for spin polarization induced in

OSCs are not fully understood. Furthermore, it is undeniable that understanding of the interfaces of ferromagnet/organic materials is crucial for optimizing spin injection and detection in organic spintronics, however we still lack a model for explaining how hybrid organic/inorganic interfaces alter spin injection. In addition to spin transport, it is also necessary to have a deeper understanding of charge transport in organic spintronic devices. Another burning issue that needs to be resolved is whether the vertical devices probe spin transport or can be explained along the lines of (multistep) tunneling [10, 11].

3. Thesis aim and outline

In my project, C_{60} is inserted into ferromagnet/insulator/ferromagnet structures to form vertical spin transport devices to experimentally study the tunneling and possibly inter-molecular transport regime of spin-polarized carriers in C_{60} in a vertical transport geometry based on magnetic tunnel junctions (MTJs). Here MTJs with structure $Co/Al_2O_3/NiFe$ which have been well studied in numerous experiments before [2, 8, 12, 13] were used as reference to compare with MTJs which had C_{60} inserted into the tunnel barrier. By varying the C_{60} thickness, I investigated different spin-dependent transport regimes, *i.e.* direct tunneling, multistep tunneling. These C_{60}-based devices were fabricated with molecular beam epitaxy and their characteristics were mainly characterized by atomic force microscopy and magneto-current measurements at temperatures ranging from 300K to 5K.

In chapter 2, some theoretical background of processes involved in spin-dependent transport, such as different relevant transport regimes of electrons/holes, the spin relaxation mechanisms of electrons/holes in semiconductors, and conductivity mismatch is discussed. Moreover, based on the properties of C_{60}, the reasons for choosing this molecule for my

investigations will also be given. Chapter 3 provides a summary of the MTJs and their characteristics, such as the tunnel magnetoresistance (TMR) and the parameters that influence the TMR value. Chapter 4 introduces the materials, fabrication and characterization techniques that were used in my experimental work. Chapter 5 discusses the results obtained from my measurement of all the devices. Based on analysis of those results, I draw some conclusions about spin transport in C_{60} in chapter 6.

CHAPTER 2

SPIN–DEPENDENT TRANSPORT IN ORGANIC SEMICONDUCTORS

1. Carrier transport in organic crystals – band transport vs. hopping transport

We consider two types of charge transport in organic solids: band transport and hopping transport. In the band transport regime, the carrier moves as a highly delocalized plane wave in a broad carrier band (spanning a considerably energy interval) with a mean free path which is relatively large compared to the crystal lattice. In contrast, in the hopping transport regime, the carrier is highly localized and moves by hopping from site to site, being scattered at virtually every step.

Each type of transport is characterized by the magnitude and temperature dependence of the mobility [14]. As for band transport, the mobility $\mu>>1$ $cm^2V^{-1}s^{-1}$ and its temperature dependence appears as $\mu \sim T^n$ where n>1. In the case of hopping transport, the mobility $\mu<<1$ $cm^2V^{-1}s^{-1}$ and its temperature dependence appears as $\mu \sim \exp(E/-k_BT)$ where E is the activation energy of the material and k_B is the Boltzmann constant.

2. Spin injection/detection

Besides charge, electrons and holes also possess an intrinsic angular momentum called spin. There are two main techniques for electrically determining spin injection phenomena. These two techniques are based on the spin valve effect and the electrical Hanle effect.

The first principle is a so-called *polarize/analyze* approach, resulting in spin valve effects. To be more detailed, this technique is based on the difference in the density of states for spin-up and spin-down electrons in a ferromagnetic material and the relative spin orientations (parallel/anti-parallel) of the two ferromagnetic layers involved in the experiment.

In this technique, an electron (or hole) current may be manipulated as it passes through a ferromagnetic layer 1/nonmagnetic layer/ferromagnetic layer 2 structure by changing the relative spin orientations of the two ferromagnetic layers. This is similar to the optical polarization phenomenon in which the intensity of light passing through two polarizers is modulated by the relative orientations of the polarizers.

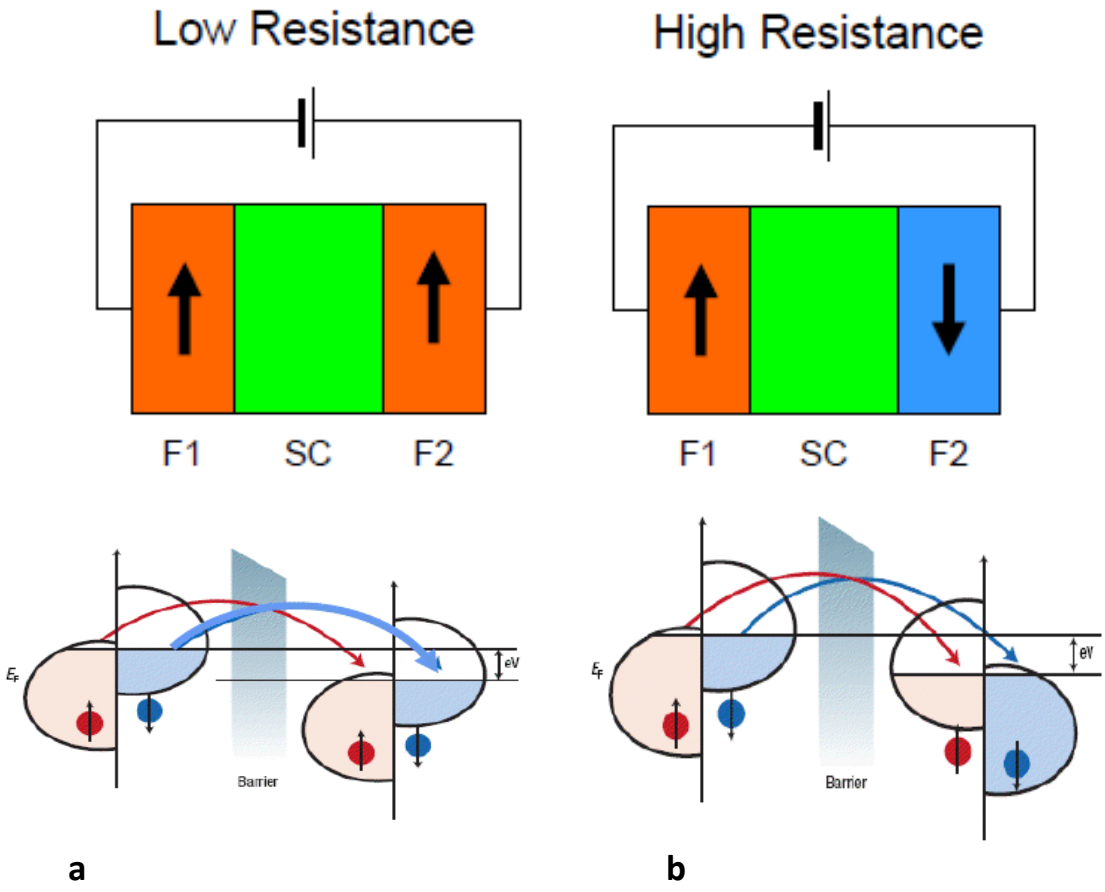

Figure 2.1: Schematic of the spin-valve effect: (a) parallel magnetizations of the magnetic contacts facilitate spin-polarized current, resulting in a low resistance state; (b) antiparallel magnetization obstructs the spin-polarized current due to lack of available states in F_2, which leads to a high resistance state.

The first ferromagnet (F_1) acts to polarize the electrons, the second one (F_2) plays the role of an analyzer. If the majority electrons in F_1 are spin-up electrons, a spin polarized current will be injected into a nonmagnetic spacer layer, and then the spin imbalance in F_1 will be transferred. If F_2 is magnetized parallel to F_1, the density of empty states for spin-up electrons will be sufficient to allow the spin-polarized current to pass, which leads to a small resistance. Nevertheless, if F_2 is magnetized anti-parallel to F_1, there will be significant scattering at the interface due to a lack of available states in the ferromagnet, resulting in a higher resistance. This change in resistance, depending on the relative orientations of the polarizer and analyzer ferromagnets, is the signature of spin dependent transport phenomena.

The second technique relies on *spin precession* which is based on the electrical Hanle effect. Experiments employing the Hanle effect involve the application of an external magnetic field to induce precession of the injected spins which diffuse from injector to collector. Varying the magnitude of this field leads to a change of the rate of precession and thus changing the total precession angle acquired by each carrier during its traversal across the device. If there is a non-zero angle between a magnetic moment **m** in a uniform magnetic field **H** then the moment will experience a torque μ:

$$\mu = \mathbf{m} \times \mathbf{H} \tag{2.1}$$

where **m** is:

$$\mathbf{m} = g(\frac{q}{2m})\mathbf{S} = g\frac{\mu_B}{\hbar}\mathbf{S} \tag{2.2}$$

where g is the Lande factor, μ_B is the Bohr magneton, q is the electronic charge of the electron or hole, **m** is the mass of the charge carrier and **S** is its spin angular momentum.

Qualitatively, the polarization is largest in zero field because all spins remain aligned. When **H** is increased, the spins precess at angular frequency $\omega_L = \frac{g\mu_B H}{\hbar}\sin\theta$, which promotes oscillations in the spin polarization at FM2 as a function of H. Second, because the transit times are broadly distributed for diffusion, the oscillatory behavior is washed out.

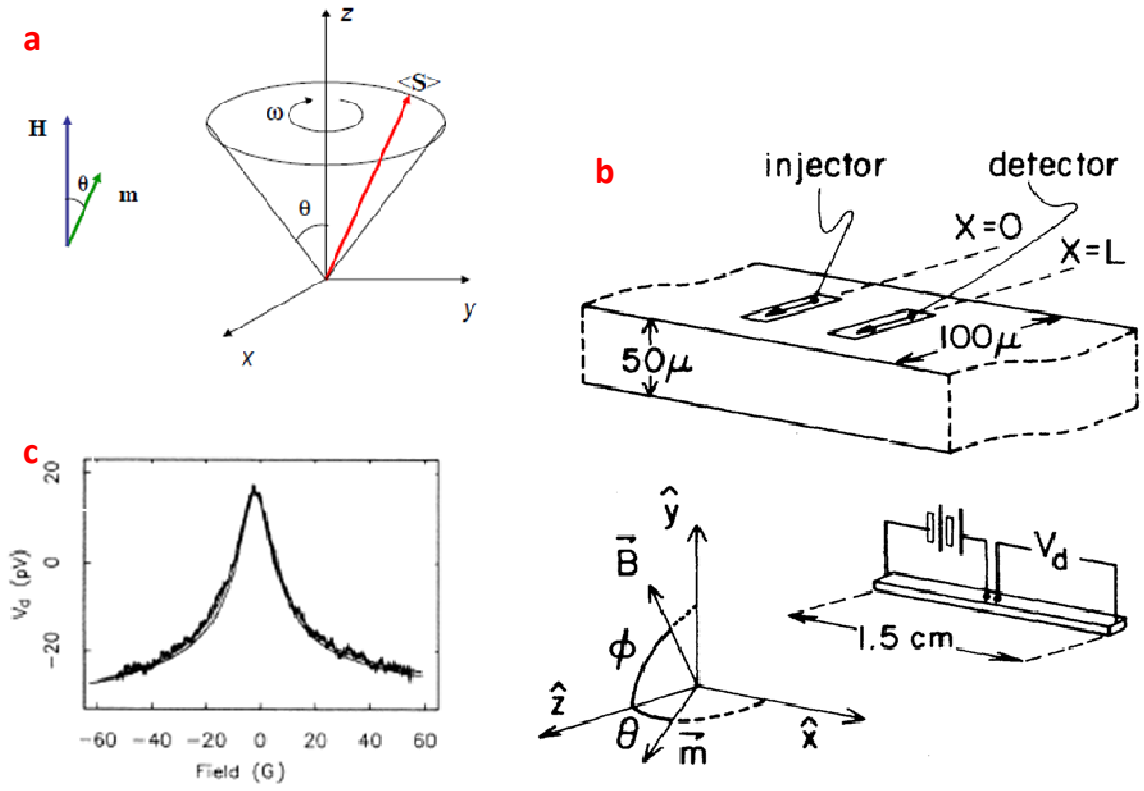

Figure 2.2: (a) Spin precession of a magnetic moment m making a non-zero angle θ with a uniform magnetic field H, (b) schematic of Hanle experiment setup and (c) obtained signal which confirmed the suppression of spin signal when the magnetic field was increased [15].

3. Spin relaxation mechanism

There are two important interactions responsible for spin relaxation of conduction electrons and holes in organic semiconductors: hyperfine interaction and spin-orbit coupling [16].

3.1 Hyperfine interaction

Hyperfine interaction is the interaction between the carrier spin and the spins of atomic nuclei. When the electron (or hole) wave function overlaps with nuclear spins, hyperfine coupling causes spin relaxation and dephasing.

The hyperfine interaction is expected to be relatively small in organic systems [17] due to several reasons. First, the interaction with the nuclei is weak in case of valance electrons (holes) (π-orbitals which have nodes in the molecular planes, minimizing the overlap between electron wave functions and the nuclei). In organic semiconductors, the hyperfine interaction mainly originates from hydrogen nuclei (isotopes ^{1}H, $I = 1/2$). Additionally, isotopes such as ^{13}C ($I=1/2$) and ^{14}N ($I=2$) also contribute to hyperfine interaction. Interestingly, ^{12}C, the most abundant isotope of carbon, does not have a nuclear spin and thus it has no contribution to the hyperfine spin relaxation. Low hyperfine interaction is desirable for devices that require long spin lifetime, such as for spin-polarized transport in organic semiconductor spin-valve devices. In contrast, significant hyperfine interaction is required to produce the interconversion of singlet and triplet electron-hole pairs for recombination magnetoresistance signals in organic semiconductor materials [18, 19].

3.2 Spin-orbit coupling

Spin-orbit coupling is the second important interaction in relaxation of carrier spins. This is the interaction between the spin angular momentum of the carrier and its orbital angular momentum. It may act like an effective magnetic field in causing spin decoherence. In an

external magnetic field, a spin will experience a torque and precess. Likewise, a spin may precess when interacting with an effective field resulting from the orbital motion. The spin-orbit interaction is categorized into three separate mechanisms: Elliott-Yafet, D'yakonov-Perel' and Bir-Aranov-Pikus. These mechanisms will be described briefly in the following paragraphs.

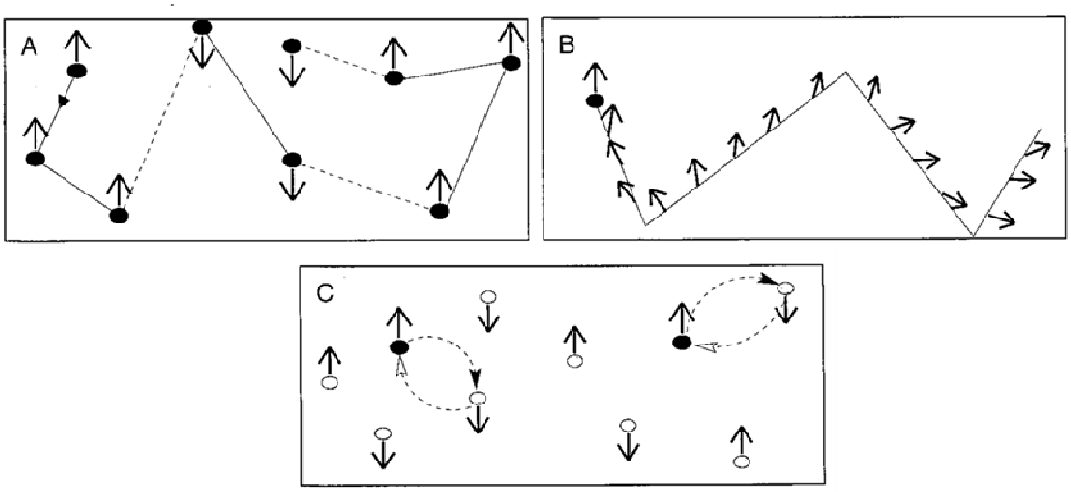

Figure 2.3: (a) Elliott–Yafet mechanism, (b) D'yakonov–Perel' mechanism and (c) Bir–Aronov–Pikus mechanism [16].

3.2.1 Elliott – Yafet mechanism

In the Elliott – Yafet (EY) spin relaxation mechanism, spin flipping is caused by the presence of impurities or phonons. In 1954, Elliott found that a conduction electron has a small chance to flip its spin via ordinary momentum scattering from impurities, boundaries, and phonons if the lattice ions induce spin-orbit coupling in the system [20]. Momentum scattering and spin-orbit coupling act on the electronic wave functions to mix the spin-up and spin-down states and thus the Bloch states (momentum eigenstates) are not pure eigenstates anymore. That results in a proportionality between the longitudinal spin relaxation time, T_1, and the momentum scattering time, τ_p. Therefore, the spin flip length ($\lambda_{sf} = \sqrt{D\tau_{sf}}$) is proportional to the mean

free path (or diffusion constant). Even for perfect crystals, the lattice ions perturb the Bloch wave functions and cause the electrons to acquire small, but finite amplitude of the opposite spin flavor and, with the assistance of momentum scattering from impurities or phonons, the spin may flip. Elliott-Yafet spin relaxation is expected to be the dominant mechanism in most metals and semiconductors.

3.2.2 D'yakonov – Perel' mechanism

The Dyakonov-Perel (DP) mechanism is due to the presence of a finite electric field in crystals without inversion symmetry [21]. As a consequence of special relativity, the electrons then experience a momentum dependent effective magnetic field and the spin precesses around this effective field. After each scattering event, the effective magnetic field changes in direction and magnitude, and thus the frequency and direction of the spin precession changes randomly, which actually suppresses the spin dephasing. Unlike in the EY mechanism in which the spin relaxation occurs *in between* the scattering events, the spin relaxation time (T_1) (and also the spin dephasing time, T_2) induced by the DP mechanism will therefore be inversely proportional to the momentum scattering time, τ_p. Therefore the spin flip length ($\lambda_{sf} = \sqrt{D\tau_{sf}}$) is independent of the mean free path because the presence of the momentum scattering rate is cancelled out by the diffusion constant [22].

3.2.3 Bir – Aronov – Pikus mechanism

The Bir-Aronov-Pikus (BAP) mechanism describes spin relaxation of conduction electrons through an exchange interaction between the electron and a hole. Overlaps between the wave functions for holes and electrons in materials are a prerequisite for the BAP mechanism. The electron-hole interaction produces an effective magnetic field which makes the electron spins precess along it. However, the hole spins may change with a rate that is much faster than

the precession frequency. If the hole spin flips (owing to strong spin-orbit interaction in the valence band also known as EY spin relaxation mechanism), electron-hole coupling will make the electron spin flip as well, resulting in spin-relaxation of electrons. This leads an increase in spin relaxation time T_1. The BAP mechanism is important for semiconductors in which the valence band has a much stronger spin-orbit coupling than the conduction band. The BAP mechanism can coexist with the EY and DP mechanisms in heavily p-doped heterostructures.

Spin-orbit interaction and hyperfine interaction have been used to describe the spin flipping process in metals and inorganic materials. However, these mechanisms cannot be applied in the same way to explain spin relaxation in our material, C_{60}, due to several reasons. Firstly, charges in OSCs propagate in very narrow bands which are created by the overlap of HOMO and LUMO of the weakly interacting molecules. For OSCs that both the valence band and conduction band are derived from π-orbitals with comparable spin-orbit coupling, BAP is not important. Additionally, since C_{60} has fcc structure which has *inversion symmetry*, Dyakonov-Perel spin relaxation mechanism can also be ruled out. Even for some organic crystals which may lack inversion symmetry, still the momentum (or velocity) of the carriers is small since the bands are very narrow. Therefore the Dyakonov-Perel mechanism is not important. Moreover, the hyperfine interaction is also expected to be weak in C_{60} since the most abundant isotopic form of carbon (^{12}C) in C_{60} does not possess a nuclear spin. Finally, the strength of the spin-orbit interaction scales as the fourth power of the atomic number, which means that spin-orbit coupling is relatively weak. However, all the reasons above finally leave Elliott – Yafet as the main spin relaxation mechanism. Thus, due to weak SO coupling, C_{60} is expected to have extremely long spin life time.

4. Conductivity mismatch

Conductivity mismatch is considered as one of the major obstacles to achieve efficient spin injection from a metal to a semiconductor. The conductivity mismatch problem arises from the huge difference between conductivities of metals and semiconductors (by orders of magnitude). In the spin injection experiment, the resistance of the device can be divided into a spin-dependent part and a spin-independent part. The electrical transport properties of ferromagnetic metals can be described in terms of a two-current model [23]. The model is based on Mott's suggestion that electron spins are predominantly conserved during scattering at temperatures lower than the Curie temperature [24]. Therefore, spin-up and spin-down electrons will travel largely independently, and carry current in parallel.

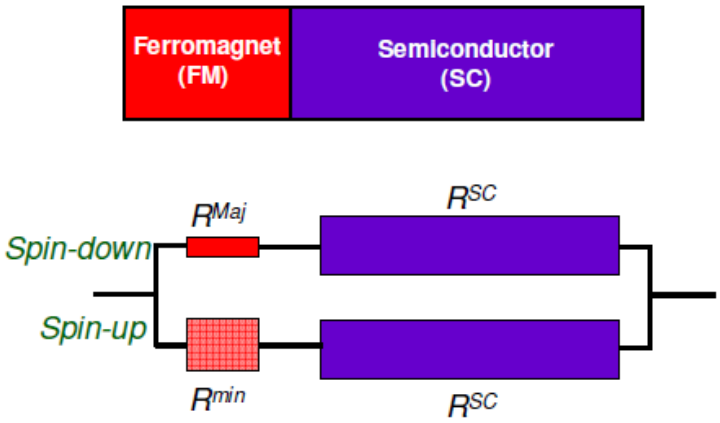

Figure 2.4: Simplistic schematic of conductivity mismatch problem in FM/SC contact.

In ferromagnetic metals, the band structures of spin-up and spin-down electrons are different; thus, the ferromagnet/semiconductor contact resistance (R^{FM}) is spin-dependent. Meanwhile, the semiconductor resistance (R^{SC}) is independent on the carrier spin, because the semiconductor is not spin polarized. When an Ohmic contact is established at the interface, the interface resistance is small and we need only consider R^{FM} and R^{SC}, where the former is much

smaller than the latter. Thus, the electron transport will be dominated by the spin-independent resistance R^{SC}, which results in the largely unpolarized electron current.

Previously, in 1987, van Son's study about electrical spin injection from a metallic ferromagnet into a normal metal introduced a splitting of the electrochemical potentials for spin-up and spin-down electrons in the region of the interface of a FM and a normal metal [25]. In 2000, based on van Son's result, G. Schmidt *et al*. provided a detailed explanation for the conductivity mismatch problem which they considered as the major obstacle for electrical spin injection from a ferromagnetic metal into a semiconductor [26]. Based on the assumption that spin-scattering occurs on a much slower timescale than other electron scattering events [25] and assuming a perfect interface without spin scattering or interface resistance (so that electrochemical potentials and the current densities are continuous), they have shown that in a diffusive transport regime the spin injection coefficient is proportional to the ratio between conductivities of ferromagnetic metal and semiconductor (σ_{sc}/σ_{fm}). Their result also explained the difference between spin injection from a FM metal into a paramagnetic metal with $\sigma_m/\sigma_{fm} \geq 1$ and a semiconductor with $\sigma_{sc}/\sigma_{fm} << 1$. According to Schmidt *et al.*, the conductivity mismatch problem seems insurmountable since a splitting of the electrochemical potentials in the ferromagnets will only be possible to attain if the resistance of the ferromagnet is of comparable magnitude to the contact resistance (which means that $\sigma_{sc}/\sigma_{fm} \approx 1$).

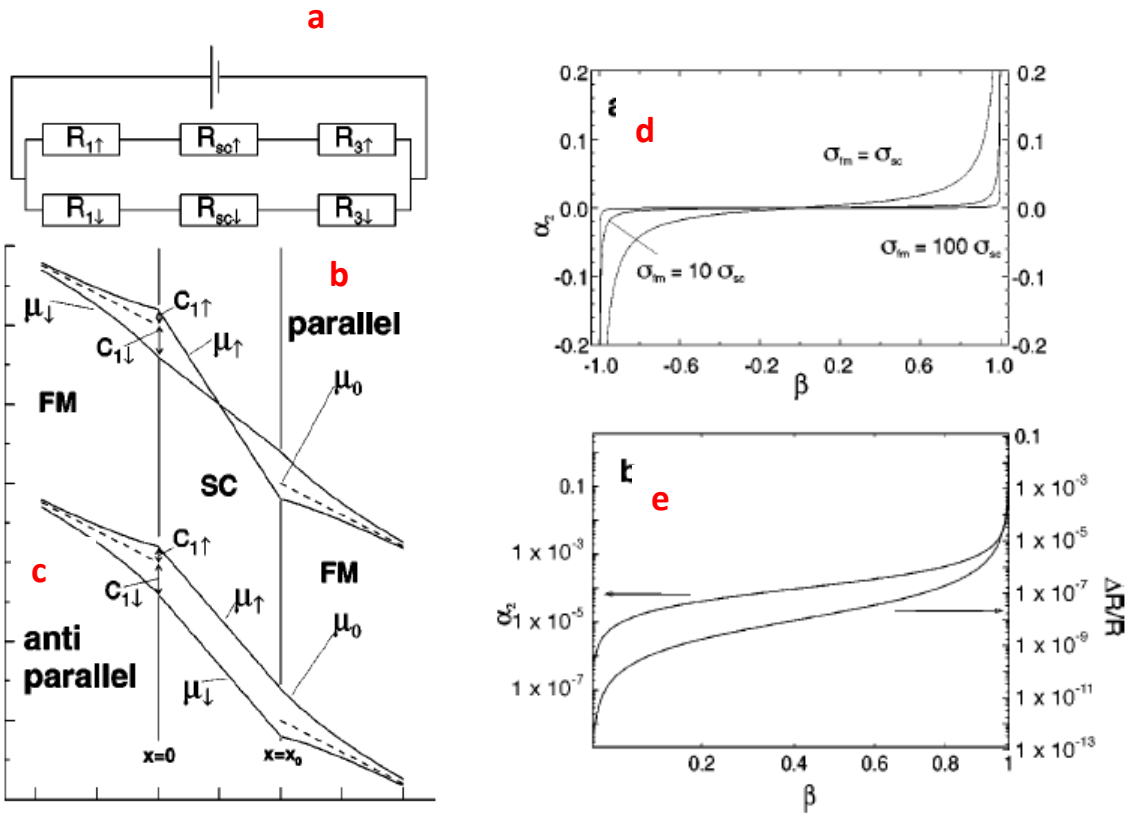

Figure 2.5: (a) Simplified picture of the two-current model for a device consisting of a semiconductor sandwiched between two ferromagnetic contacts 1 and 3. (b) and (c) show the electrochemical potentials μ in the three different regions for parallel and antiparallel magnetization of FM1 and FM3. For parallel magnetization, the slopes of $\mu_\uparrow$ and $\mu_\downarrow$ in the semiconductor are different and cross in the middle between the contacts. Because the conductivity of both spin channels is equal, this results in a (small) spin-polarization of the current in the semiconductor. In the antiparallel case, the slopes of $\mu_\uparrow$ and $\mu_\downarrow$ in the semiconductor are equal, resulting in unpolarized current flow. (d) and (e) show the dependence of spin-polarization of the current density α_2 and magnetoresistance $\Delta R/R$ on the bulk spin-polarization β of two identical ferromagnetic layers ($\beta_1=\beta_3$ in case of parallel configuration and $\beta_1=-\beta_3$ in case of antiparallel configuration).

However, later on, Rashba [27] and Smith et al. [28] independently proposed a solution to the conductivity mismatch problem. They recognized that efficient spin injection from a ferromagnetic metal into a semiconductor can be achieved due to the discontinuity of the electrochemical potentials at the ferromagnet/semiconductor interface. Thus, they inserted a low transparency tunnel barrier at the interface of the ferromagnetic metal and the semiconductor. This barrier allowed the (spin dependent) contact resistance to dominate the spin polarization α_2 rather than the ratio of conductivities σ_{sc}/σ_{fm}, which resulted in a detectable spin polarized current in the semiconductor.

CHAPTER 3

TUNNEL MAGNETORESISTIVE EFFECT

1. Magnetic Tunnel Junctions and Tunnel Magnetoresistance

Magnetic tunnel junctions (MTJs) consist of two layers of ferromagnetic materials (FM) separated by a thin insulating layer (ranging from a few angstroms to a few nanometers). This insulating layer (I) is so thin that electrons can tunnel through this barrier, resulting in a finite electrical conductance (resistance) of the component. Thus, this layer is also called tunnel barrier.

In MTJs, the tunneling current depends on the relative orientation of the magnetizations of the two ferromagnetic layers, which can be switched by applying an external magnetic field aligned parallel to the layers. This phenomenon is called *tunnel magnetoresistance* (TMR). There are several explanations for the underlying physics of TMR which have been developed by different scientists.

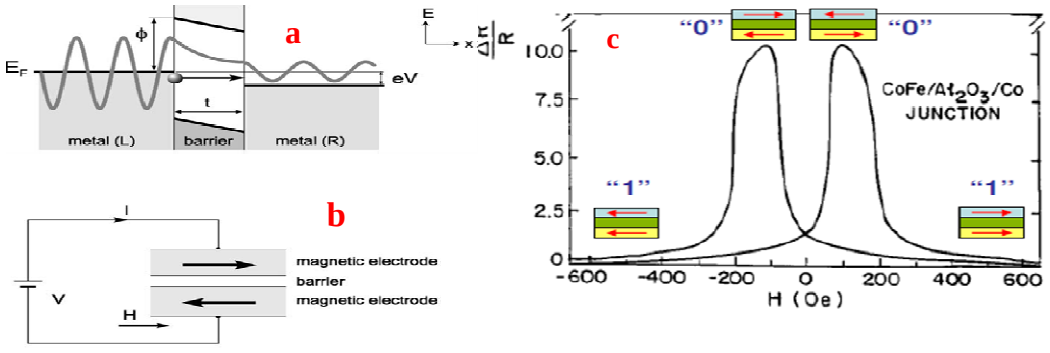

Figure 3.1: (a) The quantum tunneling effect, (b) a schematic MTJ structure: FM/I/FM and magnetocurrent measurement and (c) the TMR effect in a $Co/Al_2O_3/CoFe$ junction measured at room temperature (Ref. 2).

2. Jullière model

Jullière is the pioneering scientist who proposed spin polarized tunneling of electrons from one ferromagnetic layer to another through an insulating barrier layer and provided a possible explanation for the TMR [1]. He observed a TMR of about 14% at low temperature ($T \leq 4.2K$) and low bias voltage in Fe/Ge/Co junctions with Co and Fe electrodes, and a tunnel barrier formed with Ge which was oxidized after deposition.

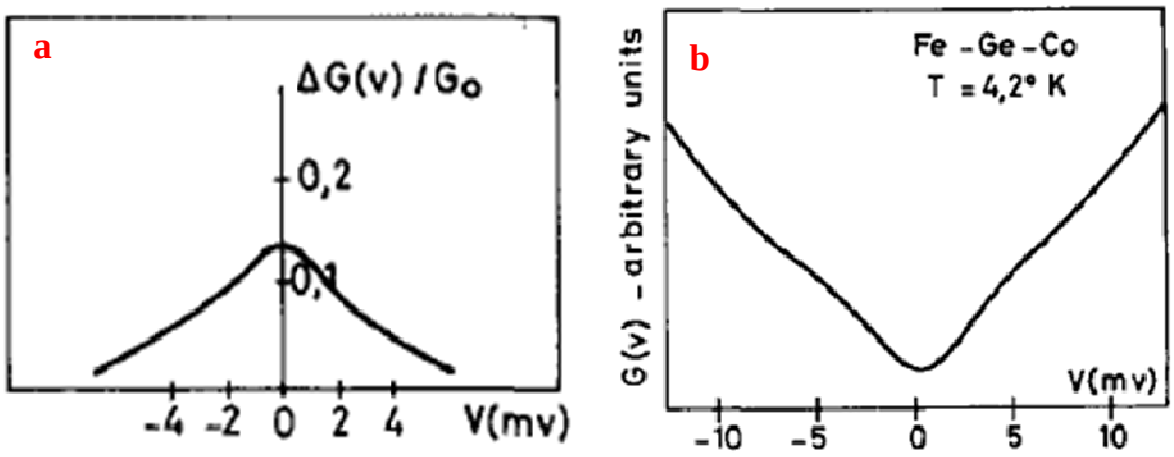

Figure 3.2: (a) The relative conductance of a Fe-Ge-Co junction at 4.2K, and (b) conductance versus bias voltage of Fe/Ge/Co junctions at 4.2K [1].

His explanation for the TMR effect [1] is mainly based on two assumptions. The first assumption is that the spins of the electrons are conserved during the tunneling process. Following this assumption, electrons with spin up and spin down will tunnel in two independent processes. To be more specific, electrons from one spin state of the first ferromagnetic layer are accepted by unfilled states of the same spin of the second layer. If the two ferromagnetic films are magnetized parallel, the minority spins tunnel to the minority states and the majority spins tunnel to the majority states. If the two films are magnetized antiparallel, the identity of the majority- and minority-spin electrons is reversed, so the majority spins of the first layer tunnel to the minority states in the second layer and vice versa.

In addition, the second assumption is that the conductance for each spin orientation is proportional to the density of states of that spin in each electrode. According to these two assumptions, the TMR can be written as follows:

$$TMR = \frac{R_{AP} - R_P}{R_P} = \frac{G_P - G_{AP}}{G_{AP}} = \frac{2P_1P_2}{1 - P_1P_2} \tag{3.1}$$

Where R_{AP} (G_{AP}) and R_P (G_P) are resistances (conductances) of the junction with antiparallel and parallel magnetizations of two ferromagnetic layers, respectively; P_1 and P_2 are the spin polarizations of two ferromagnetic layers. Up to now, this formula is still often used for estimation of the TMR values, with the addition that P_1 and P_2, besides the spin polarization of the DOS, include the tunnel transmission probablities of the different majority/minority states that are contributing to the tunnel current.

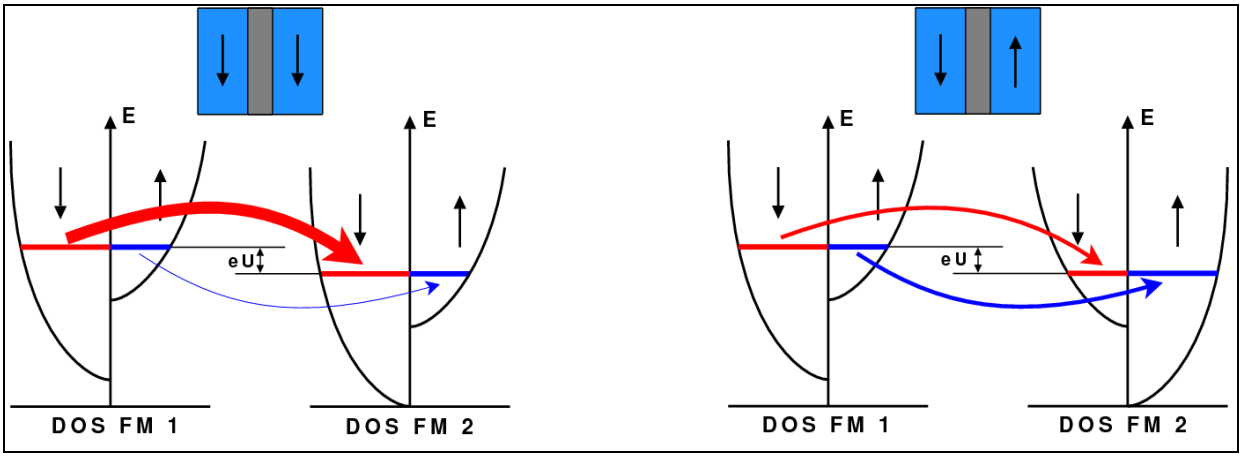

Figure 3.3: Spin subbands of two ferromagnetic layers are sketched for the parallel and antiparallel magnetization configurations.

This model successfully provided a qualitative explanation for the the strong dependence of the tunneling current on the relative orientation of magnetizations of two ferromagnetic layers with consideration of the spin polarization of two ferromagnetic layers. However, it neglected

the details electronics structure of FM materials as well as properties of tunnel barriers (electronic structure, probabilities for tunneling through the barriers). Thus, Julliere's model can not explain the dependence of TMR values on bias voltage and temperature, which show up in experimental results.

3. Slonczewski's model

In 1989, a different model for describing the spin-dependent tunneling in MTJs was proposed by Slonczewski [29]. In Julliere's explanation, the tunneling process was considered as independent of the spin of the tunneling electron, so the wave function in the barrier is treated as independent of the wave vector and spin. Slonczewski's model neglected the localized electrons and considered only the delocalized ones (free-electron approximation). In this free-electron approximation, localized electrons (d- or f-electrons) are expected not to take part significantly in the tunneling process because they are tightly bound to the atomic sites; whereas s- and p-electrons behave almost like free electrons and are expected to contribute dominantly to the tunneling.

Slonczewski considered the electrodes as well as the insulating barrier as a single quantum-mechanical system, and constructed the wave functions of spin up- and spin down electrons by solving the Schrödinger equations for the whole system. Slonczewski introduced the *effective* spin polarization of ferromagnetic electrodes:

$$P_{eff} = \frac{\left(k_{\uparrow} - k_{\downarrow}\right)\left(\kappa^2 - k_{\uparrow}k_{\downarrow}\right)}{\left(k_{\uparrow} + k_{\downarrow}\right)\left(\kappa^2 + k_{\uparrow}k_{\downarrow}\right)} \tag{3.2}$$

where κ is the extinction coefficient in barrier region, $k_{\uparrow}, k_{\downarrow}$ represent the wave numbers of electrons in the majority- and minority spin bands. The TMR is expressed as:

$$TMR = \frac{G_P - G_{AP}}{G_{AP}} = \frac{2P_{eff}^2}{1 - P_{eff}^2} \tag{3.3}$$

In Slonczewski's model, the TMR not only depends on the spin polarization of the two ferromagnetic electrodes, but also on the barrier potential height of the insulating layer. This model also took the energy dependence of electronic structure of materials into account. However, it provided only qualitative and semi-quantitative explanation of TMR.

4. Temperature dependence and bias dependence of TMR effect

The dependence of the TMR values on temperature and bias voltage has been observed in a large number of experimental studies. As the temperature and applied bias increase, the TMR values of MTJ decrease. Up to date, there are several models which have been proposed to explain the temperature and bias dependence of TMR effect.

4.1 Bias dependence

In most MTJs, the TMR magnitude decreases with increasing bias voltage, which was first observed in Julliere's experiment (Figure 3.2a). In order to explain this phenomenon, in 1997, Zhang et al. proposed a mechanism in which bias dependence of the TMR and junction resistance (R_J) of MTJs was accounted for by the spin excitations localized at the interfaces between the magnetic electrodes and the tunnel barrier [30]. In this publication, Zhang gave the definition of "zero bias anomaly" and "hot electrons". Zero bias anomaly is defined as the rapid decrease of junction resistance when the applied bias ranges from -150 mV to 150 mV. Hot electrons are defined as itinerant tunnel electrons with excess energy above the Fermi level (due to applying bias voltage). According to Zhang, when applying bias voltage to MTJs, electrons from the first ferromagnetic layer tunnel through the tunnel barrier to the second ferromagnetic layer as hot electrons. These hot electrons may lose their energy due to producing collective

oscillations of local spin at the interface between tunnel barrier and magnetic electrodes (or emitting a magnon in short) and then flipping the electron spin. Thus, when the applied bias is increased, more magnons will be emitted, thereby the TMR values decline. Moreover, this model was also confirmed by experiments performed by Moodera in 1998 [13].

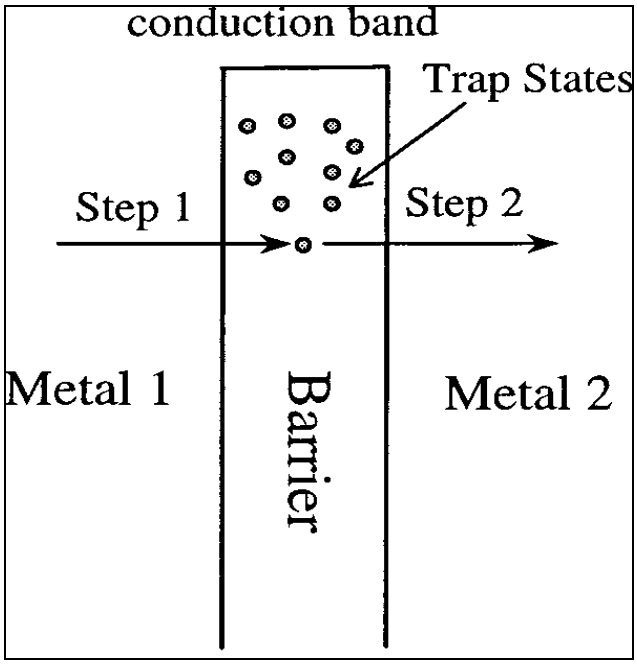

Figure 3.4: Schematic view of the two-step tunneling via defect states

Additionally, in 1998, J. Zhang and R.M. White proposed the two-step tunneling model to better understand the strong dependence of the resistance and TMR of MTJs on bias and temperature [31]. The authors suggested a thermal activation process in which localized defect states in the tunnel barrier are thermally generated. The excitation of electrons from these states will create available states for two-step tunneling (Figure 3.4). In this model, the bias dependence of the TMR in MTJs was ascribed to T_{eff} factor – effective barier temperature. They assumed that the defect states in the barrier are uniformly distributed and can be described by Fermi-Dirac function:

$$f(E) = \frac{1}{1+\exp\left[\left(E_c - E\right)/kT_{eff}\right]} \tag{3.4}$$

where E is the energy level of the defect state, E_c is the energy level of the barrier conduction band edge, *k* is the Boltzmann constant, and T_{eff} is the effective barrier temperature. Equation (3.4) states that the density of available states increases exponentially as the energy level increases. It means that the two-step tunneling current increases quickly at an increased bias voltage. Therefore, the increase of bias voltage leads to the decrease of TMR. This model was also support by experimental results from R. Jansen and J. S. Moodera [12].

4.2 Temperature dependence

The TMR values of MTJs decrease with increasing temperature. Shang et al [32] suggested a model in which temperature change not only has influence on elastic, spin-polarized tunneling but also affects a spin-independent tunneling as well as electrodes' polarization. They assumed that the tunneling spin polarization *P* decreases with increasing temperature due to spin-wave excitations, as does the surface magnetization. Thus the tunneling spin polarization and the interface magnetization followed the same temperature dependence, the Bloch $T^{3/2}$ law.

$$\begin{aligned} P(T) &= P_0\left(1-\alpha T^{3/2}\right) \\ M(T) &= M_0\left(1-\alpha T^{3/2}\right) \end{aligned} \tag{3.5}$$

Fitting parameter α provided a satisfactory explanation for the temperature dependence of TMR. In addition, inelastic scattering which does *not* flip the spin, such as electron–phonon scattering, possibly causes the reduction of TMR in the presence of localized states in the barrier.

Furthermore, the two-step tunneling model [31] mentioned in section (a) could also explain the temperature dependence of the TMR beside its bias dependence. It is due to the

assumption that the electrons from localized defect states can be activated thermally and these states will create available states for two-step tunneling.

Additionally, the reduction of the TMR with temperature was also explained by spin flip scattering by magnetic impurities in the barrier [33]. In 2001, Vedyayev *et al* [33] showed that when the temperature was increased, the number of electrons contributing to this process increased resulting in the drop of TMR.

Besides, the TMR effect has also been observed to be dependent of spin polarization of two ferromagnetic layers, properties of tunnel barrier, electronic structure around the interfaces between the ferromagnetic electrodes and the tunnel barrier.

CHAPTER 4

FABRICATION AND CHARACTERIZATION

1. Materials

1.1 Ferromagnetic materials – Cobalt (Co) and Nickel Iron (NiFe)

Co and $Ni_{81}Fe_{19}$ (further abbreviated simply as NiFe) are popular choices for MTJ electrodes. NiFe is one of the highest quality soft magnetic materials. It has a high permeability ($\mu=10^5 - 10^6$) and a small coercivity (a 15-nm NiFe layer has coercivity of about 5 *Oe*). In contrast, Co is known as a common hard magnetic material. It has a relatively low permeability and a large coercivity (a 8-nm Co layer has coercivity of about 22 *Oe*). The different coercivity between Co and NiFe provides a "window" for switching the orientation of the magnetizations of these two layers, which is a key factor to obtain TMR.

1.2 Tunnel barrier – Aluminum Oxide (Al_2O_3)

Various materials have been studied as candidates for the insulating barrier, including AlN[34] and MgO[35-37]. However, aluminum oxide is still the most widely used material for the tunnel barrier of MTJ because it can be formed easily and reliably.

Amorphous aluminum oxide is an electrical insulator (electrical conductivity $10^{-10} - 10^{-12}\ mho/m$) but has a relatively high thermal conductivity (~30 *W/mK*). Its melting point is about 2000 ^{o}C[38]. The dielectric constant ε of the Al_2O_3 barrier is smaller than that of bulk Al_2O_3, which is around 4.5–8.9 at room temperature (around 295 K). The typical height of the tunnel barrier is about 2 eV.

The Al_2O_3 tunnel barrier is very thin (~2 *nm*) and the tunneling resistance critically depends on this barrier's thickness so that small variations in the Al_2O_3 thickness lead to large variations in the resistance. Thus, in addition to being free of pinholes and very smooth, the

tunnel barrier must be extremely uniform. In our fabrication process, aluminum oxide layers are formed by deposition of a thin Al layer (~1.5 *nm*) followed by in situ oxidation using an oxygen plasma. This process helps to improve the quality of the insulating layer. Direct deposition of Al_2O_3 may possibly create some pin holes in the layer. Whereas the Al_2O_3 unit cell is about 30% larger than that of metallic Al, an Al layer with pinholes can yield a pin-hole-free tunnel layer after being fully oxidized. Besides, Al on Co grows much more smoothly than Al_2O_3, which has been proven by AFM measurements. Thus, the barrier width is more uniform.

1.3 Buckminsterfullerene – C_{60}

In 1985, Buckminsterfullerene was first prepared by Harold Kroto, James Heath, Sean O'Brien, Robert Curl and Richard Smalley at Rice University. Later on, Kroto, Curl, and Smalley were awarded the 1996 Nobel Prize in Chemistry for their roles in the discovery of buckminsterfullerene and the related class of molecules, the fullerenes.

The C_{60} molecule consists of 60 carbon atoms, arranged as 12 pentagons and 20 hexagons. Its shape is the same as a soccer ball, with the average diameter of 7.09 Å [39]. If the π-electron cloud which is associated with the carbon valence electrons is taken into account, the outer diameter of C_{60} can be estimated as about 10.34 Å where 3.35 Å is the estimated thickness of the π-electron cloud around carbon atoms of C_{60} [40]. The electron affinity of gaseous C_{60} is about 2.65 eV, in the solid state it is 4.0 eV [41]. The calculated HOMO–LOMO band gap of C_{60} varies between 1.55 – 1.85 eV [42]. In vacuum, crystalline C_{60} sublimes at about 350^{o}C [43]. The electrical resistivity of pure C_{60} (and also of C_{60}/C_{70} mixture) is about ~10^{14} Ω·cm at room temperature [44, 45].

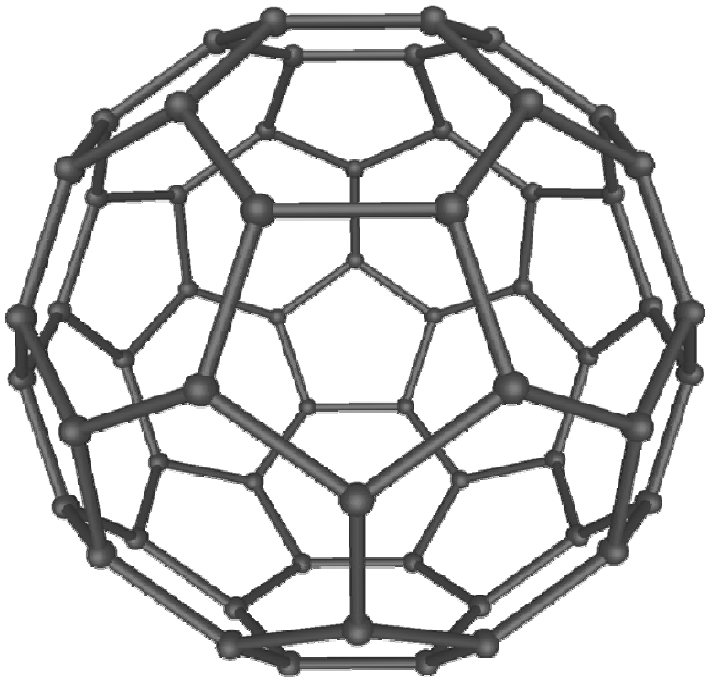

Figure 4.1: C_{60} molecule.

In my thesis project, C_{60} molecules were inserted into MTJ structures to form vertical spin transport devices. C_{60} is an attractive material for organic spintronics due to several reasons. Firstly, the lack of hydrogen in C_{60} might lead to a very weak hyperfine coupling (the C_{12} nuclei have zero spin) which is believed to cause the organic magnetoresistance (OMAR) effect [46] and is a source for spin relaxation and dephasing. Secondly, C_{60} has a high electron affinity (about 4.0 eV) which results in small energy barriers at the interfaces. A larger energy barrier at the interface implies a smaller amount of injected carriers at a given voltage, which means that we need to apply higher voltage to the device to obtain clear signals. Meanwhile, high bias, in turn, will reduce the spin polarization of the injected current. In my devices, the Fermi level of the metal could be aligned close to the LUMO of C_{60}, so that it could be easier for spin injection. Last but not least, C_{60} molecules are highly symmetric and crystallize easily, such that it is possible to grow epitaxial, crystalline layers of C_{60} onto ferromagnetic substrates.

2. Fabrication

In our experiments, we prepared series of MTJs consisting of NiFe/Al_2O_3/Co and NiFe/C_{60}/Al_2O_3/Co. The samples with an Al_2O_3 tunnel barrier were prepared in molecular beam epitaxy system (DCA-Metal-600) using shadow mask (Figure 4.1 and 4.2a, respectively).

2.1 Molecular beam epitaxy

Our samples with high quality thin films of metal, oxide and semiconductor were fabricated using Metal-600 molecular beam epitaxy (MBE) system from DCA Instruments. The molecular beam epitaxy system consists of two chambers: the main chamber (growth/ evaporation chamber) and a small loadlock chamber. First, substrates are loaded when the loadlock chamber is opened to the air while the main chamber remains under vacuum. After that, only the small chamber needs to be evacuated. This greatly reduces the contamination of the vacuum in the growth chamber as well as increasing the output of processed wafers. Using a turbopump, the pressure in loadlock chamber can be pumped down to 1×10^{-7} Torr. When the pressure in the loadlock chamber is reduced to lower than 5×10^{-7} Torr, the valve between loadlock chamber and main chamber can be opened and the substrate is introduced to the main chamber.

The base pressure in the main chamber is maintained at about $2x10^{-10}$ Torr (ultra high vacuum condition – UHV) using a cryopump, during depositions additional pumping capacity is provided by a liquid nitrogen cooled baffle. When we start depositing layers onto the substrate, the pressure may be increased to 10^{-9} – 10^{-8}Torr. The essence of the MBE concept is that the growth surface is kept clean by the UHV; thus the vacuum environment surrounding the growing layer must be kept as low as possible to avoid contamination that might affect electrical

properties, film morphology and also whether or not epitaxial growth takes place [47]. All layers were deposited inside the main chamber by e-beam evaporation.

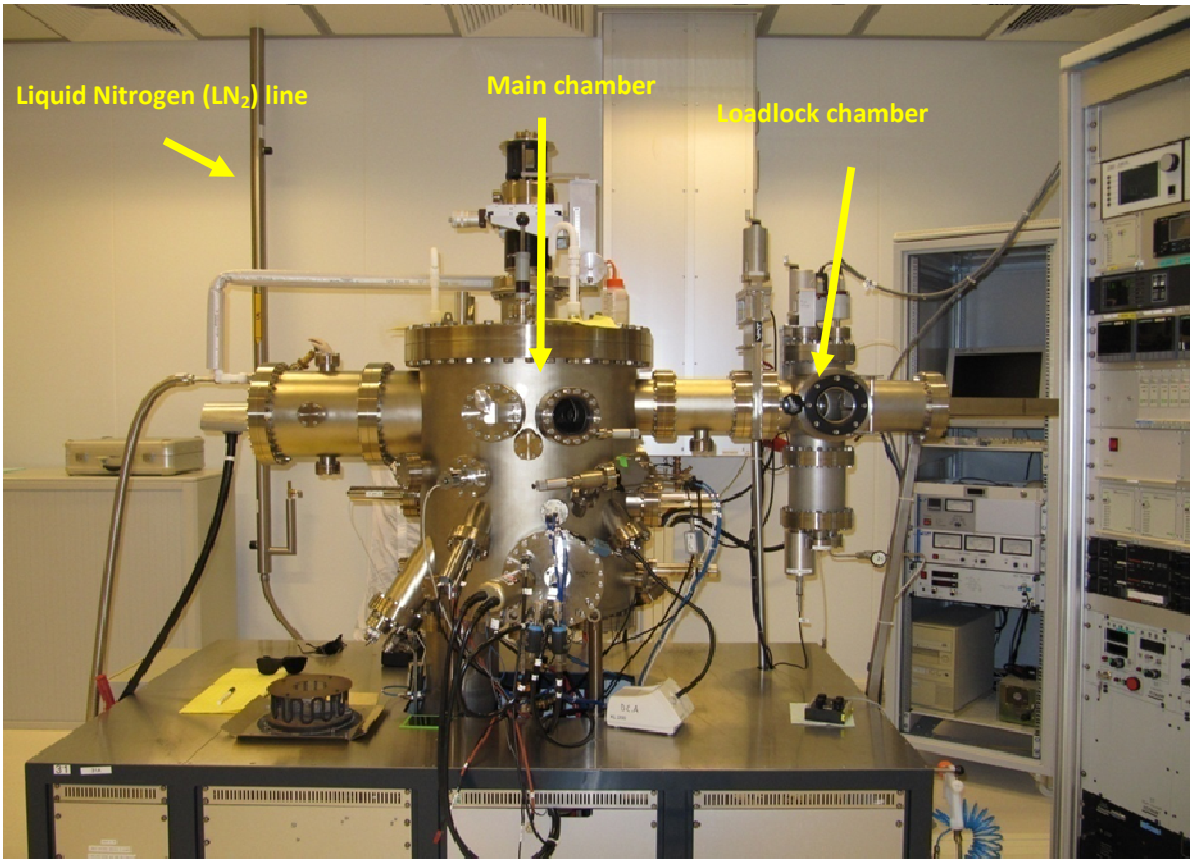

Figure 4.2: Molecular beam epitaxy system (DCA-Metal-600)

Besides, the oxidation of Al which is used to obtain high-quality tunnel barrier is done in the load-lock chamber using plasma oxidation. During this oxidation process, O_2 is introduced to the small chamber and 800 V is applied between two electrodes to generate plasma. The plasma oxidation process took 30 minute under constant pressure (~100 mTorr).

2.2 Fabrication process

The fabrication process contains 5 steps as following. All steps were carried out in the main chamber (except for the plasma oxidation process).

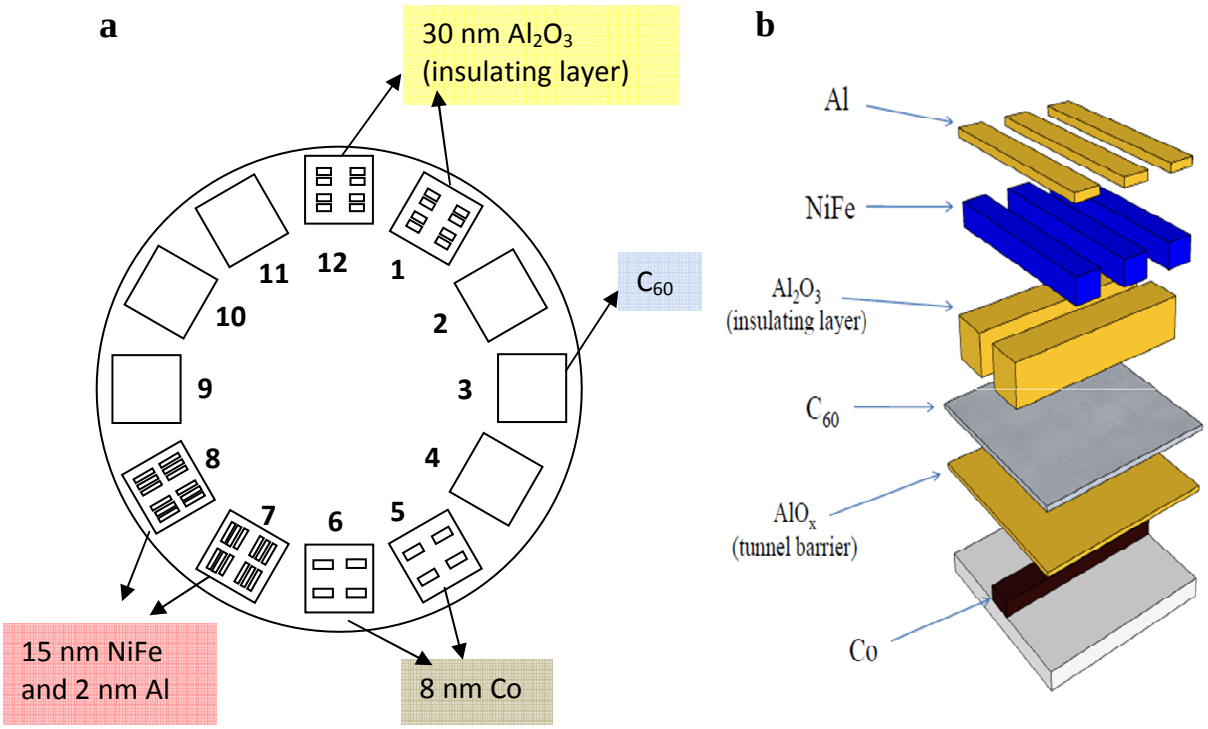

Figure 4.3: Schematic of (a) shadow mask which was used for MTJ fabrication and (b) steps of fabrication process.

▪ Initially, the two substrates were put in position 5 and 6 where Co layer was evaporated onto single crystal Al_2O_3 substrate for 2-3 minutes (depends on the deposition rate). The thickness of this layer is 8 nm, which is calculated based on calibration of Co deposition in DCA before. The area of deposited Co layer is 4.8×1.9 mm^2, which is determined by the shadow mask.

▪ After that, they were moved to position 2 and 3 where a 1.5 nm Al layer is deposited all over the samples. This is followed by plasma oxidation for 30 minutes (at constant pressure 100 mTorr). After this process, the aluminum layer is oxidized and has an approximate thickness of 2.0 nm. The thickness of the oxidized Al layer has been corrected for the 30% expansion of Al upon oxidation into Al_2O_3.

- Afterwards, the two samples were moved to position 4 and 3. Position 4 was closed (Figure 4.3a) so C_{60} layer was only formed with thermal evaporation at 400°C only at position 3. The thickness of this layer varies from one to several C_{60} monolayers, which depends on the evaporation time. After this step, we have two different samples with and without C_{60} layer on the top of Al_2O_3 tunnel barrier.
- Subsequently, at position 1 and 12, a 30 nm Al_2O_3 layer is evaporated. This layer acts as a protective layer which prevents bottom and top electrodes contact at unexpected area. Each of this insulating layer had area of 3,3×1.4 mm^2.
- Finally the second ferromagnetic layer (15 nm NiFe) is evaporated at position 7 and 8. At the same position, a 2 nm thin Al cap is deposited. This cap prevents the NiFe layer from oxidizing. The area of NiFe and Al layers is 4.5×0.3 mm^2.

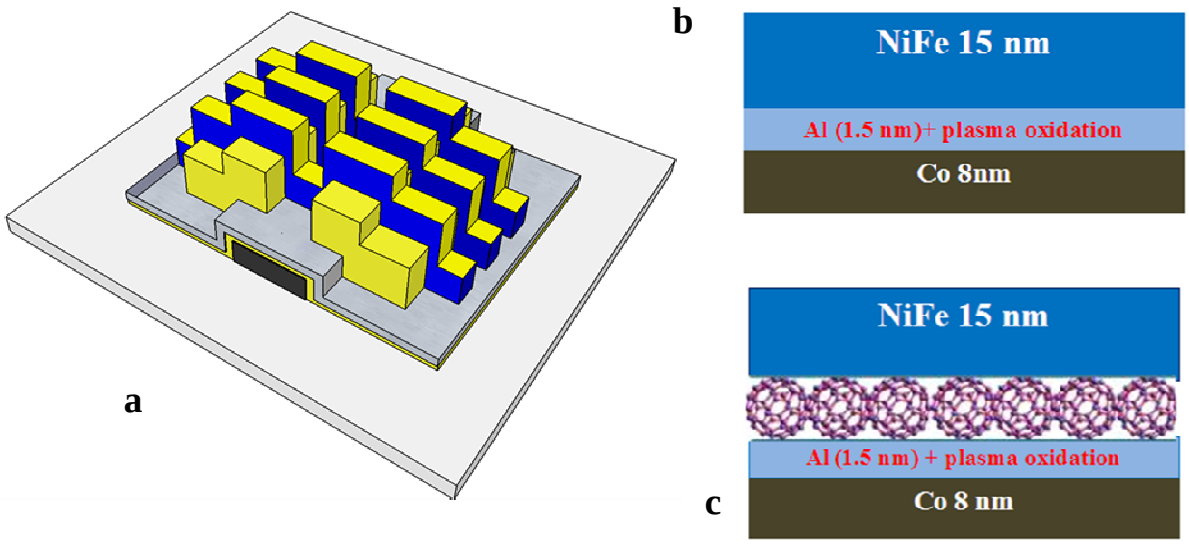

Figure 4.4: Schematic structure of (a) fabricated devices, (b) standard MTJ and (c) hybrid MTJ.

After this process, we have one sample with C_{60} in the barrier (hybrid MTJ) and one standard sample (without C_{60}) as a reference (Figure 4.4b and 4.4c). Each sample contained 12 junctions which has area of approximately 0.25×0.3 mm^2.

3. Characterization

These samples were mainly characterized with magneto-current measurements at temperatures ranging from 300K to 5K.

Magneto-transport measurements were performed in an measurement setup which consists of a Bruker electromagnet, a liquid helium flow cryostat, a temperature controller, a Keithley 2400 source meter and a measurement computer which is connected with all instrumentss (Figure 4.5a). In these measurements, the electric current through the MTJs is measured as a function of magnetic field (with fixed applied voltage) and bias voltage (at fixed applied magnetic field) at wide range of temperatures (from room temperature down to 5K).

First, the sample is put in the center of the Bruker magnet which can generate magnetic fields up to 2 Tesla. Via a computer program, a fixed bias voltage (~20 mV) and a varying magnetic field (usually ranging from -200 Oe to 200 Oe) which enables switching between the parallel and antiparallel configurations of the two electrodes of the MTJs were applied to the sample, then a current could be measured with the Keithley 2400 source meter. Similarly, by applying fixed values of the magnetic field, the voltage–current curves of the MTJs can be measured in the parallel and antiparallel magnetization configurations by varying the applied bias and obtaining the current change. The schematic of the measurement setup is shown in Figure 4.5b.

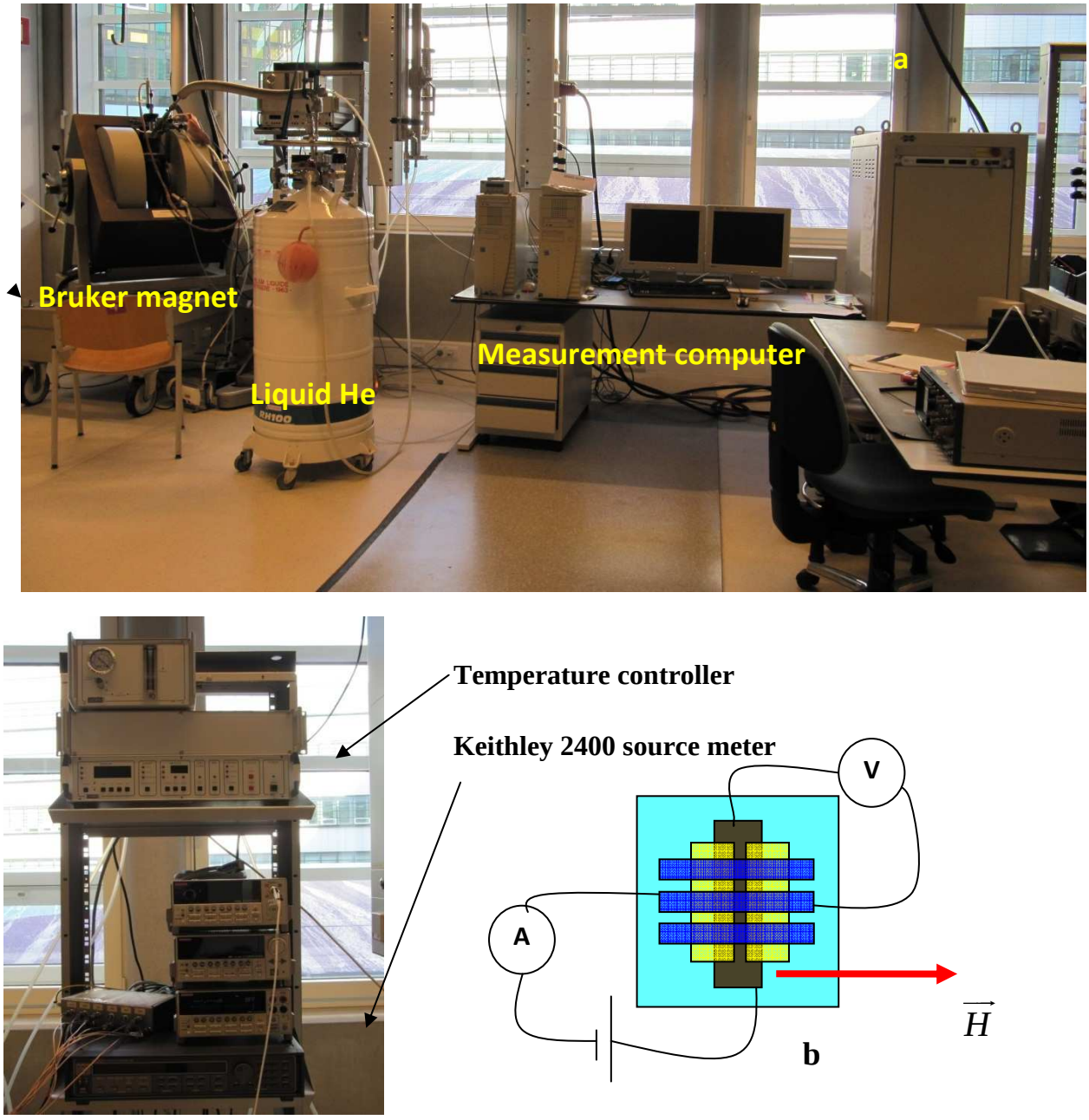

Figure 4.5: (a) Measurement system and (b) schematic of magnetotransport measurement setup.

The sample can be measured in vacuum and in a He environment. Low temperature can be achieved by a flow of liquid He along the sample chamber which is filled with He gas, which allows for temperatures as low as 5 K. Higher temperatures than room temperature, up to 350 K, can be achieved by heaters.

CHAPTER 5

RESULTS AND DISCUSSION

In this chapter, I will present the results obtained from measurements on a Co/ Al_2O_3/NiFe junction (standard MTJ, without C_{60}) compared to Co/Al_2O_3/*x* nm C_{60}/NiFe junctions (hybrid MTJs, with *x* nm C_{60} with *y* ranges from 0 to 20 nm), followed by a discussion on the interpretation of these results.

The magnetic field dependence of the junction resistance (magnetoresistance) was measured with a four-point measurement technique with different applied bias voltages at various temperatures (ranging from room temperature to 5K). The schematic of four-point measurement technique has been provided in chapter 4. In this magnetocurrent measurement, the bias voltage was kept fixed between two contacts on the cross-bar structure (top- and bottom electrodes of the junction), while the current sourced through the other two contacts was recorded as a function of the external magnetic field. The tunnel magnetoresistive effect which showed up in most of my MTJs was calculated using the relation (3.1):

$$\mathrm{TMR} = \frac{R_{ap} - R_p}{R_p} \cdot 100\%$$

where R_p and R_{ap} are the junction resistances which were measured at parallel and antiparallel magnetization of two ferromagnetic layers, respectively.

In addition to magnetocurrent measurements, the current-voltage dependence of all devices was also measured with a four-point probe technique at different temperatures and applied fields. In the current-voltage dependence measurement, the magnetic fields were set to such values that either a parallel- or antiparallel magnetization configuration of the top- and bottom ferromagnetic layers was obtained. The conductance-voltage (*dI/dV*) and bias

dependence of the TMR, which are determined from these *I-V* characteristics, provide information about the (spin dependent) tunneling mechanism through the dual Al_2O_3- and C_{60} tunnel barriers, where the population of (spin polarized) intermediate states in the latter are of special interest. The *I-V* curves measured at parallel magnetization of the two ferromagnetic layers are labeled as I_p in the following, while the others, measured at antiparallel magnetization of these two layers, are referred to as I_{ap}. Similarly, the conductance-voltage curves, which were obtained by numerical differentiation (d/d*V*) of I_p (I_{ap}), are called parallel (antiparallel) conductance G_p (G_{ap}). The bias dependence of the TMR value was derived from I_p and I_{ap} using the following formula:

$$\mathrm{TMR(V)} = \frac{I_p - I_{ap}}{I_{ap}} \cdot 100\%$$

1. Structure and morphology

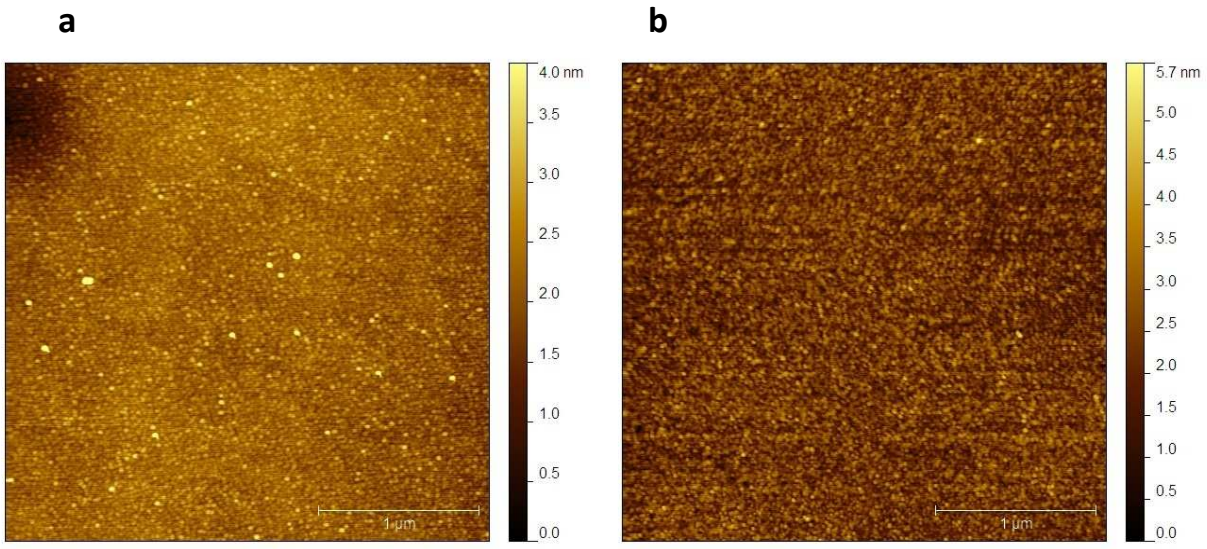

Figure 5.1: Atomic force microscopy image of (a) Al_2O_3/Co/substrate with rms~0.3 nm and (b) C_{60}/Al_2O_3/Co/substrate with rms~0.6 nm.

Figure 5.1 shows the atomic force microscopy images of (a) a 2 nm Al_2O_3 layer deposited on 8 nm Co (which was previously deposited on a single crystal Al_2O_3 substrate) and (b) a 7 nm C_{60} layer subsequently deposited onto these 2 layers. The typical rms roughness of Al_2O_3/Co was around 0.3 nm while typical rms roughness of C_{60}/Al_2O_3/Co was around 0.6 nm. The thickness of these layers was determined *in situ* by a quartz crystal monitor. The relatively small roughness of Al_2O_3/Co is in agreement with previous studies [48]. This small roughness suggests that we have an Al_2O_3 layer with uniform thickness which is very good for studying tunneling transport. The good quality AlOx barrier was also confirmed by transmission electron microscopy (TEM) measurement (Figure 5.2).

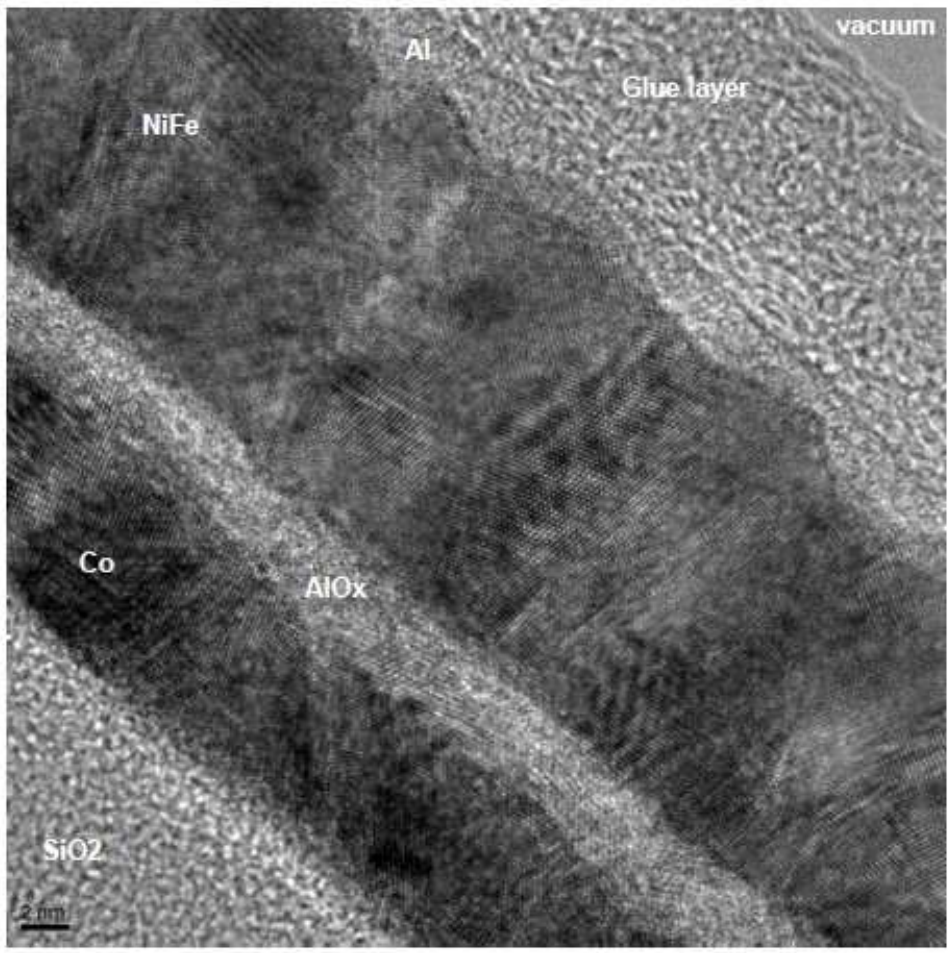

Figure 5.2: TEM image of a standard junction.

2. C_{60} thickness dependence and bias dependence at room temperature

We obtain clear and reproducible positive tunnel magnetoresistive effects at different temperatures and applied bias voltages for MTJs with 0–7 nm C_{60} (Figure 5.3a). The TMR measurements show that the junction resistance increases sharply upon switching the electrode magnetizations from a parallel configuration to an antiparallel configuration. The curves show a plateau when the field value is in between the values for reversing the magnetizations of NiFe and Co (antiparallel magnetization). The lower coercive field is ascribed to the NiFe electrode, while the higher one is ascribed to the Co electrode.

The strong dependence of the junction resistance on the magnetization configuration is consistent with spin polarized tunneling. The fact that a significant TMR effect was observed (through measurement) in most of our MTJs (0–7 nm C_{60}) is the first evidence for a spin-dependent tunneling mechanism of electrons through the barrier composed of Al_2O_3 and C_{60} layers. It is also clear that the TMR values of hybrid MTJs are smaller than that of a standard MTJ, and that the TMR decreases monotonically with the thickness of the C_{60} layer (Figure 5.3b). At room temperature, the standard MTJ shows a TMR of about 15.6% while hybrid MTJs with 0.5 – 7 nm C_{60} layer have TMR values ranging from 15.6 to 2.9 %. As for the MTJ with 0.5 nm C_{60}, it is noticeable that its TMR value is essentially the same as that of the standard MTJ (both 15.6%). Because 0.5 nm C_{60} is less than one monolayer of C_{60} (which is about 1 nm), the C_{60} molecules do not completely cover the junction area so that the current will flow mostly in regions where there is no C_{60}. Thus, the device behavior will be dominated by the regions where NiFe is in direct contact with Al_2O_3. Indeed, the device characteristics (temperature and bias dependence of TMR and conductance) for the device with 0.5 nm C_{60} closely follow those of a

standard MTJ. The behavior of MTJs with increasing C_{60} thickness will be discussed in more detail at a later stage.

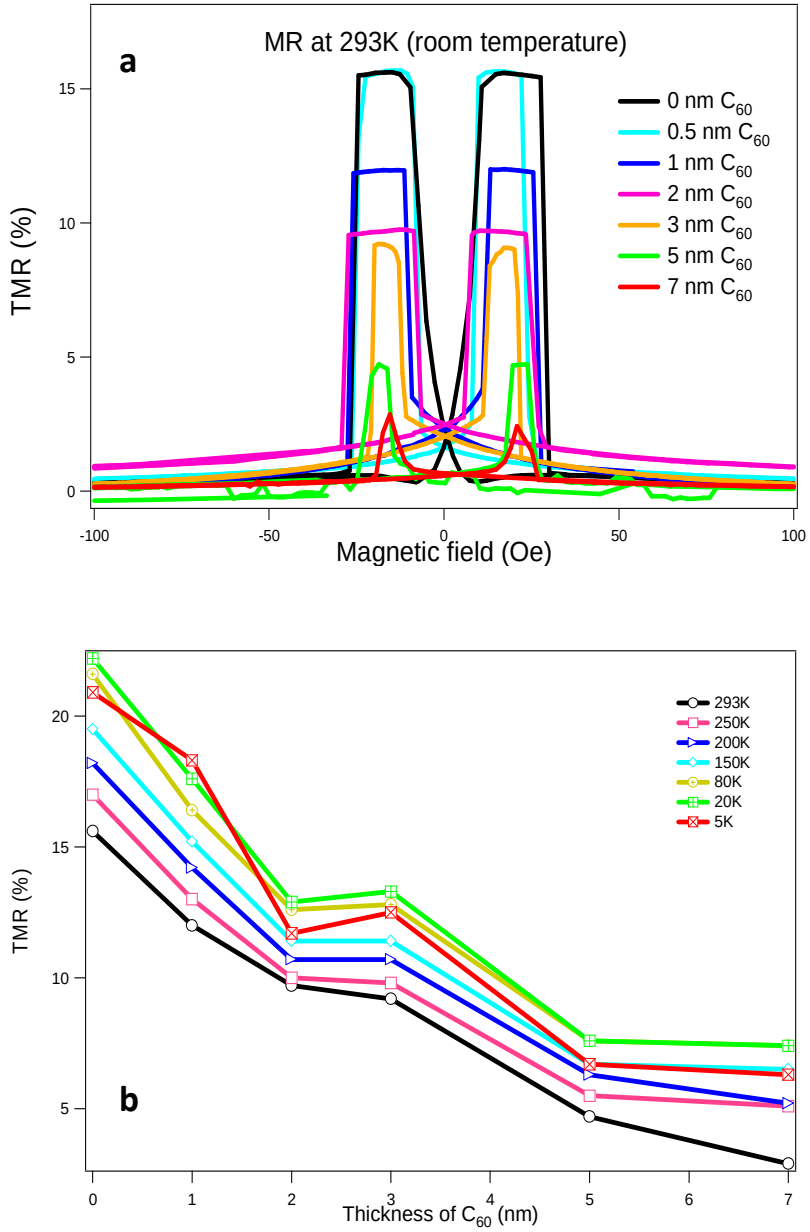

Figure 5.3: (a) TMR plotted as a function of magnetic field. These data were measured with applied voltage 20 mV at room temperature; (b) TMR value vs. C_{60} thickness at temperature varying from 293K down to 5K.

As expected, the resistance of all MTJs is strongly dependent on the barrier width (2 nm Al_2O_3 and *x* nm C_{60}). The thicker the C_{60} layer, the higher the junction resistance. In figure 5.4, the junction resistance at parallel configuration (R_P), measured at a temperature of 293K and a bias of 20 mV, was plotted as a function of the thickness of the organic layer (C_{60}). The logarithmic increase of R_P versus the thickness of the C_{60} layer (note that a logarithmic scale is used in the plot) is consistent with the exponential behavior of the tunneling mechanism [49]. Fitting the resistance of all MTJs (*d*=0–7 nm, *d* is the thickness of C_{60} layer) with $R \sim \exp(\beta d)$ yields the parameter β=1.0465 (Figure 5.4).

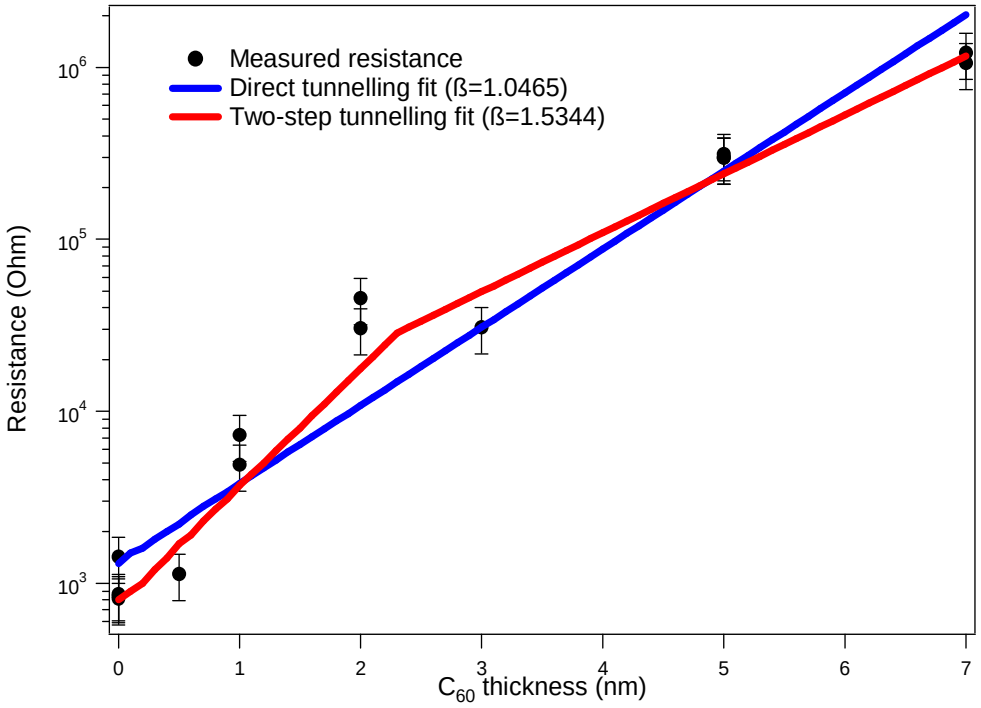

Figure 5.4: Resistance of the junctions as a function of C_{60} thickness. Fitting the resistance of all MTJs (*d*=0–7 nm, *d* is the thickness of C_{60} layer) with $R \sim \exp(\beta d)$ yields the parameter β=1.0465 (blue); fitting the resistance of MTJs *d*=0–2 nm with $R \sim \exp(\beta d)$ and the resistance of MTJs *d*=2–7 nm with $R \sim \exp(\beta d/2)$ yields the parameter β=1.5344 (red).

However, it is noticeable that for MTJs with d=0–2 nm C_{60} the junction resistance increase more strongly than that of MTJs with d=2–7 nm C_{60}. Analogous to the behavior of Alq_3-based devices as described in reference [50], we can identify the onset of 2-step tunneling and discriminate between transport dominated by direct tunneling or 2-step tunneling from the resistance of the junctions as a function of C_{60} thickness. Schoonus *et al.* suggested that the transition between the two regimes was marked by a crossover between an exponential increase of R_p with the thickness of the tunnel barrier (R~exp(βd) or J~exp(-βd) where d is the barrier thickness) for direct tunneling and an exponential increase of R_p with *half* the thickness of tunnel barrier (R~exp($\beta d/2$) or J~exp(-$\beta d/2$)) for two-step tunneling. Here by assuming that there is only forward hopping so that the direct tunneling current is equal to the two-step tunneling current at the intermediate site. Thus, via calculation, the total transmission probability for sequential tunneling events will be maximum for sites that reside roughly halfway in the C_{60} barrier. Fitting the junction resistance of MTJs which have d=0–2 nm with R~exp(βd) and the junction resistance of MTJs which have d=3–7 nm with R~exp($\beta d/2$) yield parameter β=1.5344. Interestingly, for d=2–3 nm, their values of junction resistance are in the same order of magnitude. This is possibly the transition point between direct tunneling and two-step tunneling mechanism. When C_{60} thickness is increased, multi-step tunneling will dominate the transport mechanism. The reason for the dominance of multi-step tunneling as C_{60} thickness increases will be discussed later along with the explanation for bias dependence characteristics of all MTJs.

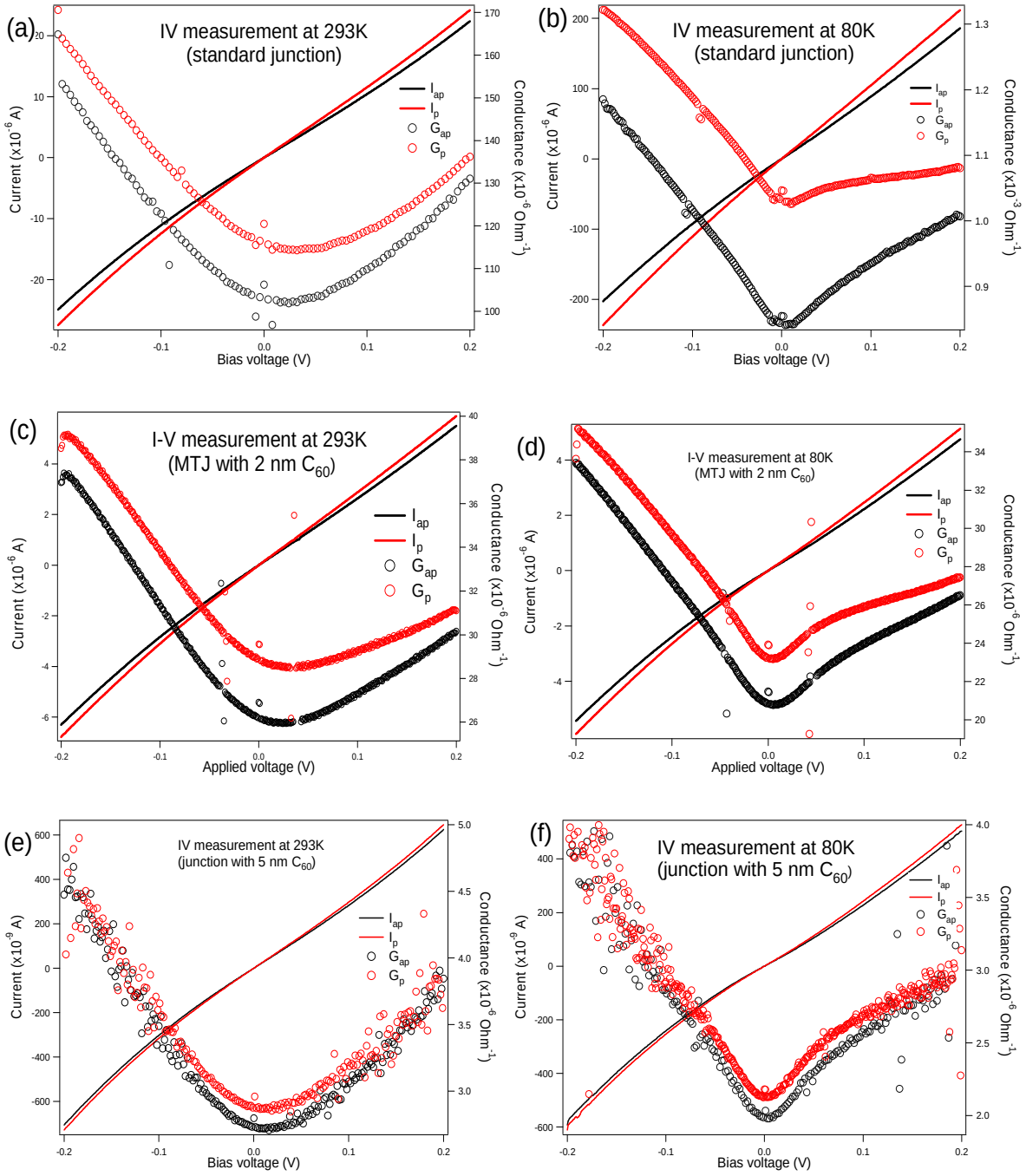

Figure 5.5: *I-V* (lines, left axes) and *dI/dV* (circles, right axes) curves for standard MTJ measured at room temperature (a) and at 80K (b), and those of MTJ with 2 nm C_{60} and 5 nm C_{60} measured at room temperature (c), (e) and at 80K (d), (f).

Figure 5.5 shows several current-voltage (*I-V*) and conductance (*dI/dV*) curves of a standard MTJ and MTJs with 2 nm C_{60} and 5 nm C_{60}, measured at room temperature and at 80K. These curves are typical for measurements of the *I-V* characteristics of all MTJs (0–7 nm C_{60}) at various temperatures (from room temperature down to 5K). All *I-V* curves are non-linear, consistent with tunneling as the main transport mechanism of electrons through the Al_2O_3 and C_{60} barriers. The *dI/dV* curves are distinctly asymmetric with respect to the bias voltage, as expected in an MTJ with different electrode materials (Co and NiFe). The bias-asymmetry of the conductance curves increases upon reducing thermal smearing at low temperature, and a dip develops at low bias voltages ("zero bias anomaly"), which was discussed in chapter 3. The difference between I_p and I_{ap} as a function of increasing applied bias shows that the tunneling transport through the barriers of my junctions is spin-dependent throughout the whole bias range.

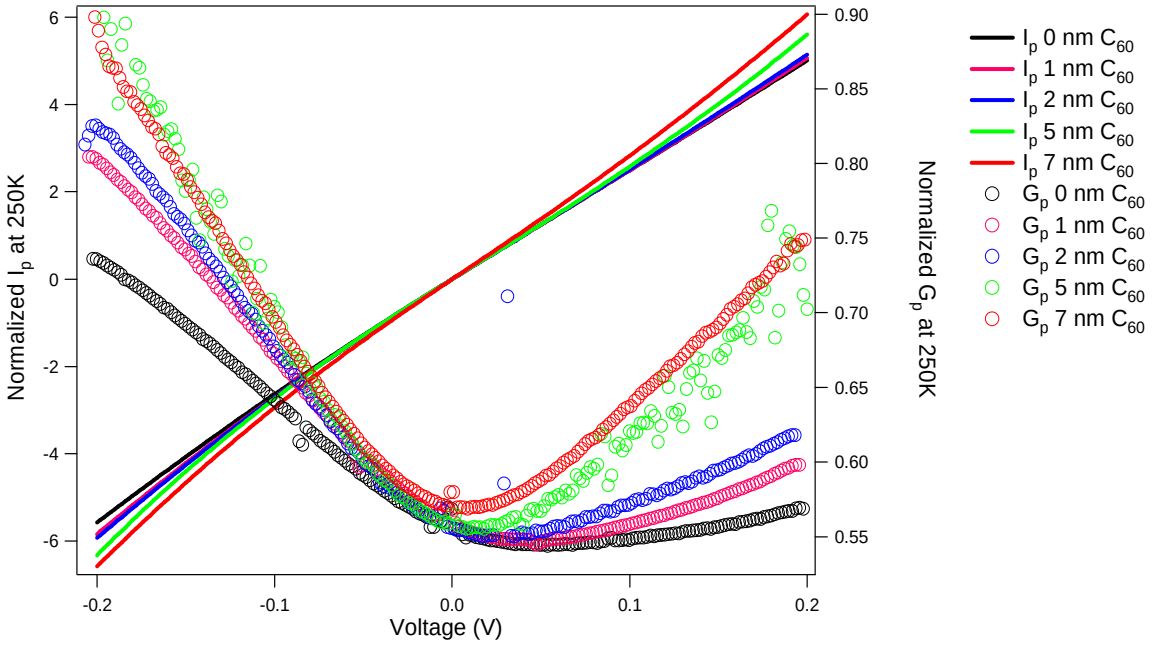

Figure 5.6: Normalized *I-V* (lines, left axis) and normalized *dI/dV* (G_P, circles, right axis) curves for MTJs with 0–7 nm C_{60} at 293K (room temperature). *I-V* curves and *G(V)* curves were normalized by dividing by their maximum values at near zero bias.

In addition, upon increasing the C_{60} thickness, the *I-V* curves become more non-linear while the *dI/dV* becomes more parabolic-like, meaning that both the current and conductance become more strongly dependent on bias (Figure 5.6). It indicates different barrier heights for the Al_2O_3 and the C_{60} sides of the barrier. At room temperature, the *dI/dV* curves do not show a zero bias anomaly (near linear *I-V* characteristics when the applied voltage is close to zero), which is suggestive of elastic tunnelling of electrons through Al_2O_3 and C_{60} barrier. The stronger bias dependence of the current/conductance of MTJs with thicker C_{60} layers can be explained by a lower effective barrier height, which is due to the fact the the LUMO level of C_{60} is close to the Fermi level of Co and NiFe. Meanwhile, fitting the tunnel current of a standard MTJ with Brinkman's model [51] yields a value for the insulating barrier thickness of about 28.7 Å, , while the average barrier height between these two electrodes (at zero applied bias) of 1.68 eV. Here the conductance (*dI/dV*) of standard junction was fit with the equation (assuming that T=0K for simplicity):

$$\frac{G(V)}{G(0)} = 1 - \left(\frac{A_0 \Delta\varphi}{16\bar{\varphi}^{3/2}} \right) eV + \left(\frac{9}{128} \frac{A_0^{\,2}}{\bar{\varphi}} \right) (eV)^2$$

$$\Delta\varphi = \varphi_2 - \varphi_1$$

$$\bar{\varphi} = (\varphi_1 + \varphi_2)/2$$

$$A_0 = 4(2m)^{1/2} d/3\hbar$$

$$G(0) = \left(3.16 \times 10^{10} \bar{\varphi}^{1/2} / d \right) \exp\left(-1.025 d \bar{\varphi}^{1/2} \right)$$

Where *d* is the barrier thickness in Å, φ_1 and φ_2 are the barrier heights on two sides with zero applied voltage. The computed thickness of Al_2O_3 tunnel barrier is larger than expected (nearly 2 nm). However, it seems to be in good agreement with TEM measurement (Figure 5.2 in part 1 of

chapter 5) in which the thickness of Al_2O_3 thickness is larger than 2 nm. The reason for this difference might be because Brinkman built this model base on the assumption of T=0K for simplification (so that the authors disregarded the temperature dependence of tunnel current/conductance).

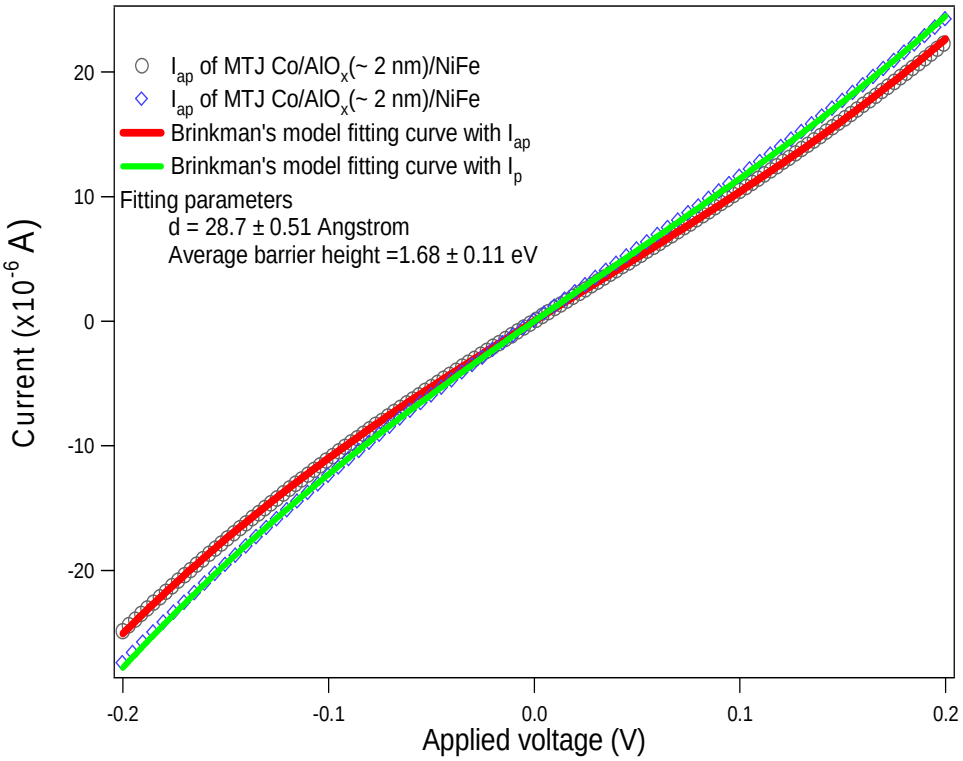

Figure 5.7: Fitting curves of tunnel current using Brinkman's model [51] yields barrier thickness of about 28.7 Å and barrier height of 1.68 eV.

The most pronounced change of the junction behavior as a function of the C_{60} thickness is the TMR, which becomes more bias dependent as the C_{60} layer thickness increases, while the maxima of the TMR curves are at positive bias value near zero bias. The asymetry of the TMR curves versus bias reverses as the C_{60} thickness is increased, and becomes quite large for the junctions with the thickest C_{60} layers (Figure 5.8). As for MTJs with 0–3 nm C_{60}, their TMR(V)

curves are nearly parabolic and only show slightly asymmetric behavior, with a little faster decrease when increasing the applied bias in the positive direction. In contrast, TMR(V) curves for MTJs with 5 and 7 nm C_{60} present clearly stronger asymmetric shapes with more significant decrease of the TMR upon increasing the applied bias in the negative direction.

The bias dependence of the TMR of MTJs has been investigated in numerous publications before [2, 12, 13, 30-32], some of which have been reviewed in chapter 3. In general, the asymmetry can arise from dissimilar electrodes, due to the fact that the states participating in the tunneling are different for forward bias (positive applied voltage) and reverse bias (negative applied voltage). When positive voltage is applied, the chemical potential of NiFe electrode is shifted upward in relation to that of Co electrode. Electrons at the Fermi level and below that of the NiFe electrode will tunnel into states above the Fermi level in the Co electrode. When negative voltage is applied, electrons at (and below) the Fermi level of the Co electrode will tunnel into states above the Fermi level in the NiFe electrode. The dissimilar interfacial electronic states at the two electrode/barrier interfaces plays an important role as well. Apart from these general issues, the thickness of the C_{60} layer (which does not impact the electronic structure at the interfaces) clearly also affects the TMR, especially at negative bias. This point will be further addressed below.

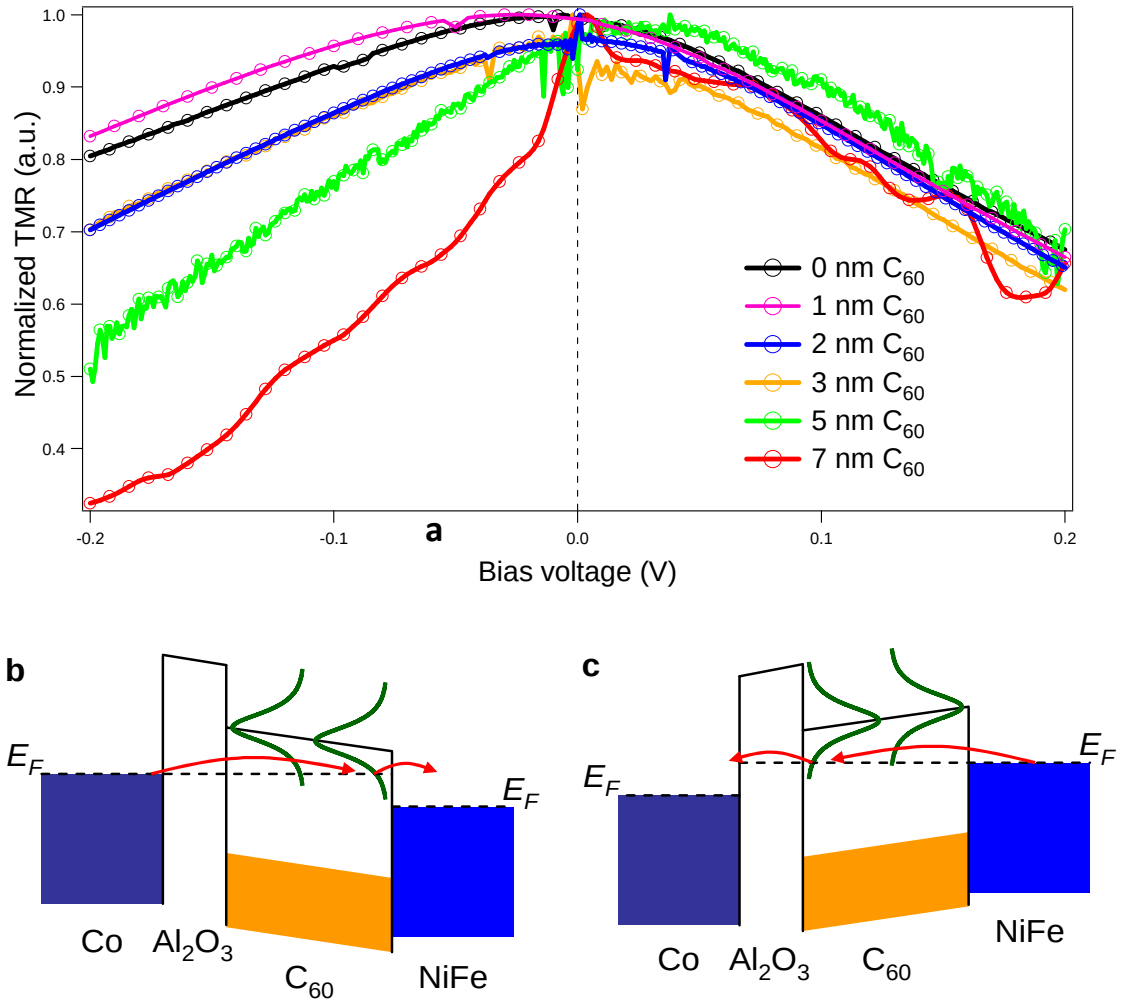

Figure 5.8: (a) Normalized bias dependence of TMR of all junctions measured at room temperature (293K). All bias dependence TMR curves are normalized by their maximum values at around zero bias. (b) and (c) Schematic of energy level with Gaussian distribution of defect states for multi-step tunneling when negative and positive bias are applied, respectively.

Moreover, as mentioned in part 5.1, the roughness of C_{60} layer (deposited onto Al_2O_3/Co) is higher than that of Al_2O_3 deposited onto Co. Thus, the interface between C_{60} and NiFe will

have higher roughness than the interface between Al_2O_3/Co and Al_2O_3/NiFe. As stated in [52], interface roughness may lead to local interface magnetic fields (stray fields) which can alter the spin polarization near the tunnel interface. In addition, for many OSCs, transport takes place as hopping in Gaussian or exponentially distributed states. The assumption of a Gaussian density of state was based on, for example, the analysis of time-of-flight experiments in OLEDs [53]. Applying a bias voltage tilts the potential within the C_{60} layer so that the DOS of "defect" states (in analogy with tunneling through a barrier with defects) will align with E_F of the electrode (Figure 5.8b). By combining these two ideas, we can find a reasonable explanation for the stronger dependence of TMR on negative applied bias. Applying a bias voltage tilts the potential within the C_{60} layer, so that DOS of defect states aligned with E_F of the electrode depends on the distanec from that electrode (Figure 5.8b). Thus, at negative (positive) bias voltages, the distribution of intermediate states shifts away from (towards) the Al_2O_3 interface (Figure 5.8b and 5.8c). Since the C_{60}/NiFe interface has a considerably larger roughness than Co/Al_2O_3 interface, the defect states which are available for two-step tunneling will be redistributed towards the C_{60}/NiFe interface at sufficiently high negative bias. Under the effect of local interface magnetic fields (stray fields) arising at C_{60}/NiFe interface, this redistribution might result in higher spin precession frequency and thus a larger reduction of the spin polarization in the defect state. If the external magnetic field which is applied to align the magnetization of the FM layers is not strong enough to cancel the stray field, this inhomogeneous field may dominate and randomize the spin orientation of electrons. Thus, the behaviors of my devices (decrease of TMR and stronger bias dependence at negative applied voltage when thickness of C_{60} layer increases) were attributed to the presence of Gaussian/exponential distribution of defect states in C_{60} and the effect of stray field at the interface of C_{60}/NiFe.

3. Temperature dependence

The junction resistance (R_P) and TMR of all junctions at room temperature are depicted in figure 5.3a and 5.4, respectively. To have a deeper look at the trends of change of R_P and TMR upon cooling, figure 5.9 is produced by normalizing the junction resistance and TMR to their values at room temperature. The junction resistance R_P and the TMR of all junctions increase significantly. Generally, R_P of all junctions monotonically increases with the decrease of temperature. Meanwhile, the TMR change follows a different trend. When the temperature was reduced from 293K to 80K, the TMR *increased* significantly and monotonically. However, upon cooling down further from 80K to 5K, the TMR *decreased* slightly.

The increase of R_P along with the decrease of temperature is understandable. To be more detailed, the R_P of the hybrid junctions increases by 30 – 65%, much faster than that of the standard junction (increase of about 20%) (Figure 5.9a). This shows that thermal activation becomes more important in the transport mechanism. Meanwhile, the TMR of hybrid junctions also increases more strongly upon cooling (from room temperature to 80K) (especially for the devices with the thickest C_{60} layers) in comparison with that of the standard junction (Figure 5.9b). The TMR of hybrid MTJs increases with about 50–150% when the temperature was lowered to 20K, while the TMR of the standard MTJ only increased by about 40% at 20K.

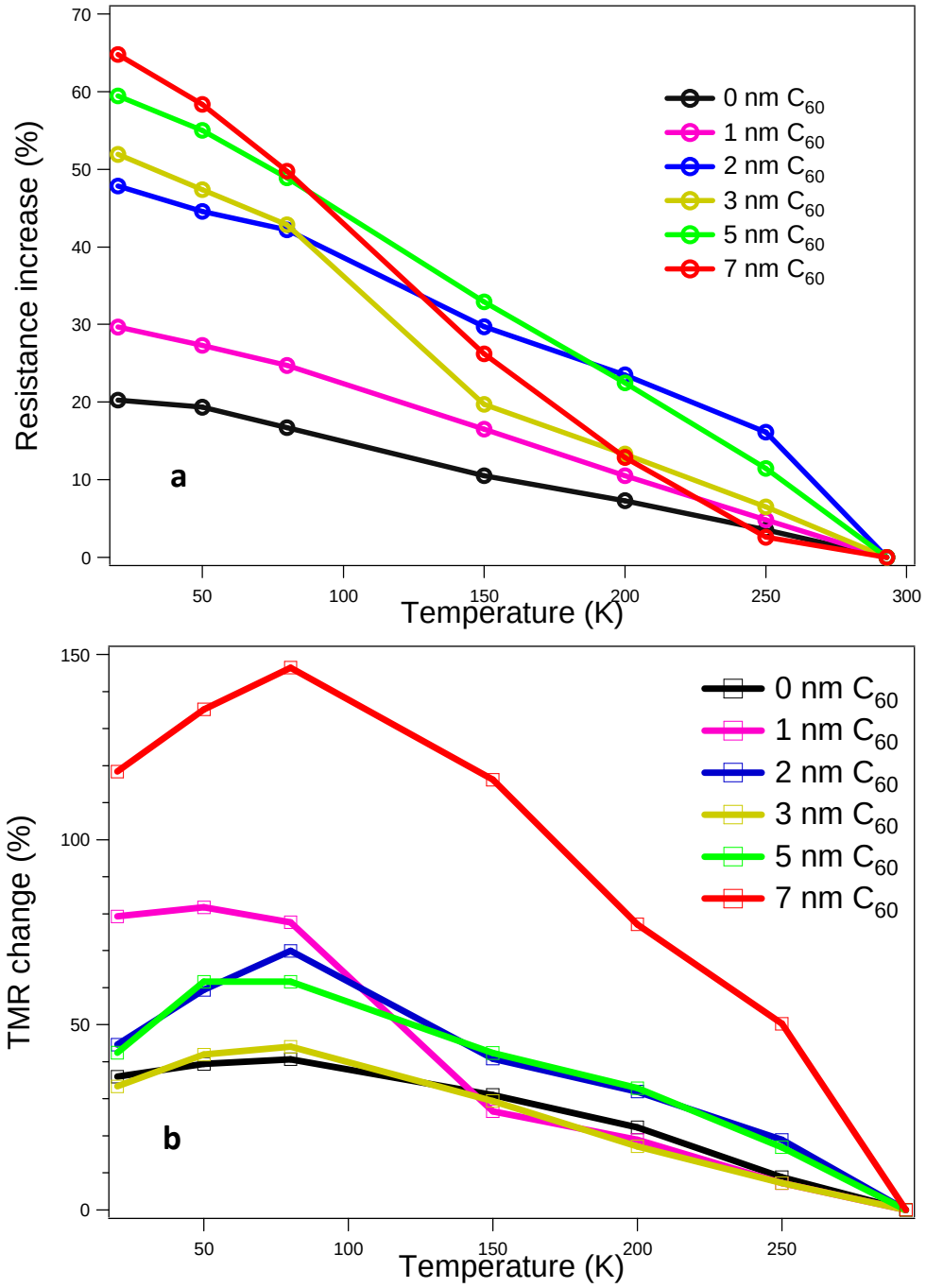

Figure 5.9: Changes of (a) junction resistance and (b) TMR vs temperature. These changes were obtained by normalizing to junction resistance and TMR values at room temperature (293K).

This behavior is analogous to Zhang's model, concerning two-step tunneling via defect states (discussed in chapter 3), with localized defect states in the tunnel barrier that are thermally activated, thereby creating available states for two-step tunneling. Thus, the significant

temperature dependence of the TMR is also understandable since the C_{60} layer is expected to have considerably more "defect" states close to the Fermi energy (Gaussian distribution, as stated in the previous part) via which thermally activated tunneling can take place than the Al_2O_3 layer. In the previous part, it has been discussed that the hybrid MTJs comprising C_{60} show a significantly stronger temperature-dependent behavior (resistance, current–voltage, conductance, TMR) than standard MTJs. It should be pointed out lastly that the large temperature dependence of R_P and the TMR rules out the possibility that metallic charge transport through metallic filaments or via pin holes is dominant.

Figure 5.10 shows the temperature dependence of the *I-V* and conductance curves of junctions with 0 and 5 nm C_{60}. Upon cooling down, the *I-V* curves of all MTJs become more nonlinear and the overall conductance decreases (curves shift downward due to higher R_P). The conductance becomes more dependent on bias when cooling down to 5K. It is noticeable that the zero-bias anomaly appears in conductance curves and also TMR curves at low temperature (5K and 20K) (Figure 5.10 and 5.11). There have been many theories for the origin of zero-bias anomaly in MTJs. However, this issue is still under debate now. According to Zhang's model which was discussed in chapter 3, the presence of the zero-bias anomaly may be because of that hot electrons, *i.e.* tunneling electrons with excessive energy above the Fermi level (due to the applied bias), lose their energy owing to the emission of magnons at the tunnel barrier/electrode interface and then flipping their spins. At low temperature, these electrons possibly need a higher applied voltage to be excited, since the thermal energy becomes smaller and thus does not contribute as much to the total energy as compared with the situation near room temperature. Therefore energy gained from the applied bias plays a more important role, which results in a more dramatic bias dependence of the *I-V*, conductance and TMR curves (Figure 5.10 and 5.11).

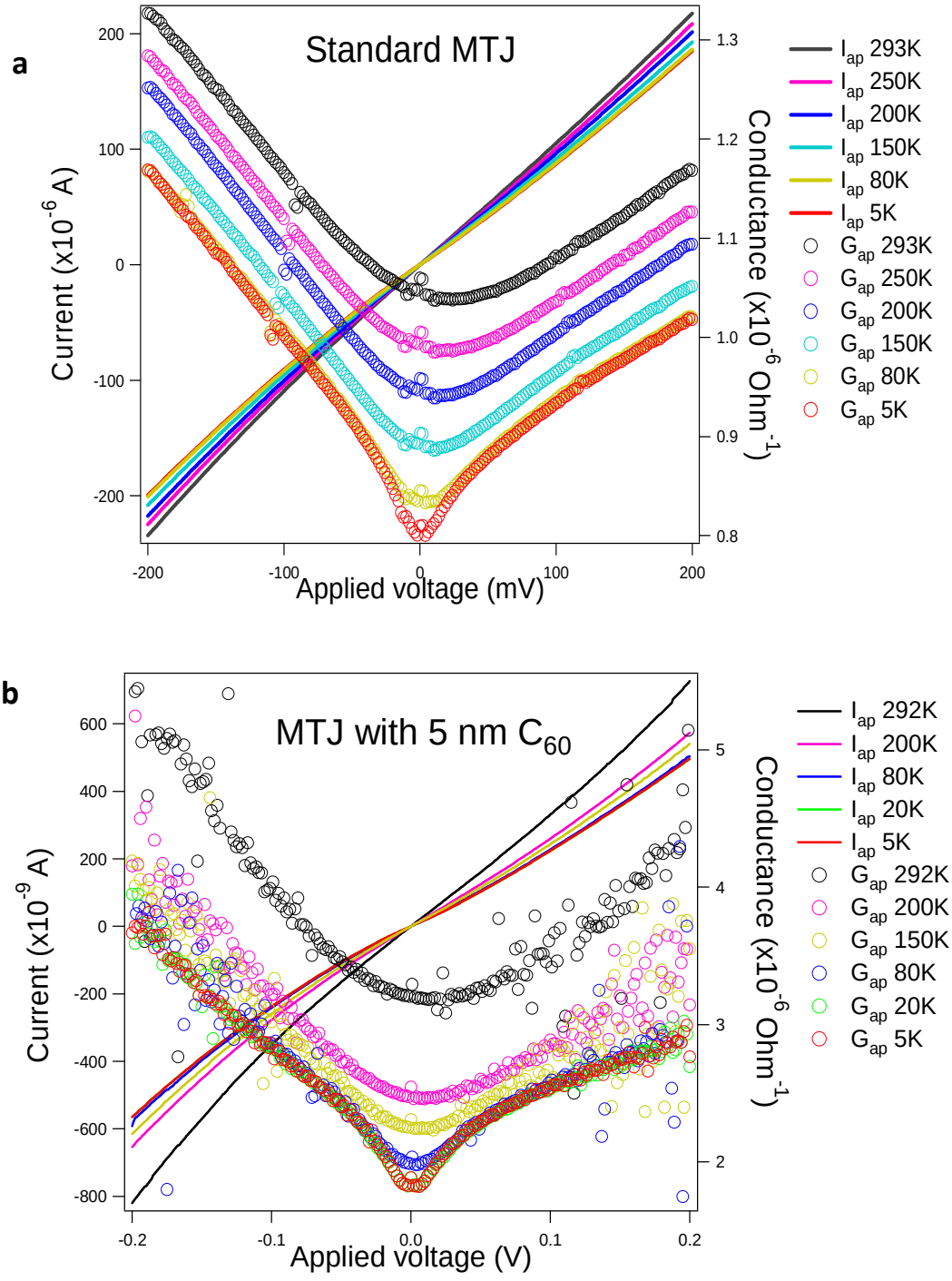

Figure 5.10: *I-V* (lines, left axes) and conductance *dI/dV* (circles, right axes) curves of junctions with (a) 0 and (b) 5 nm C_{60} measured upon cooling from room temperature to 5K.

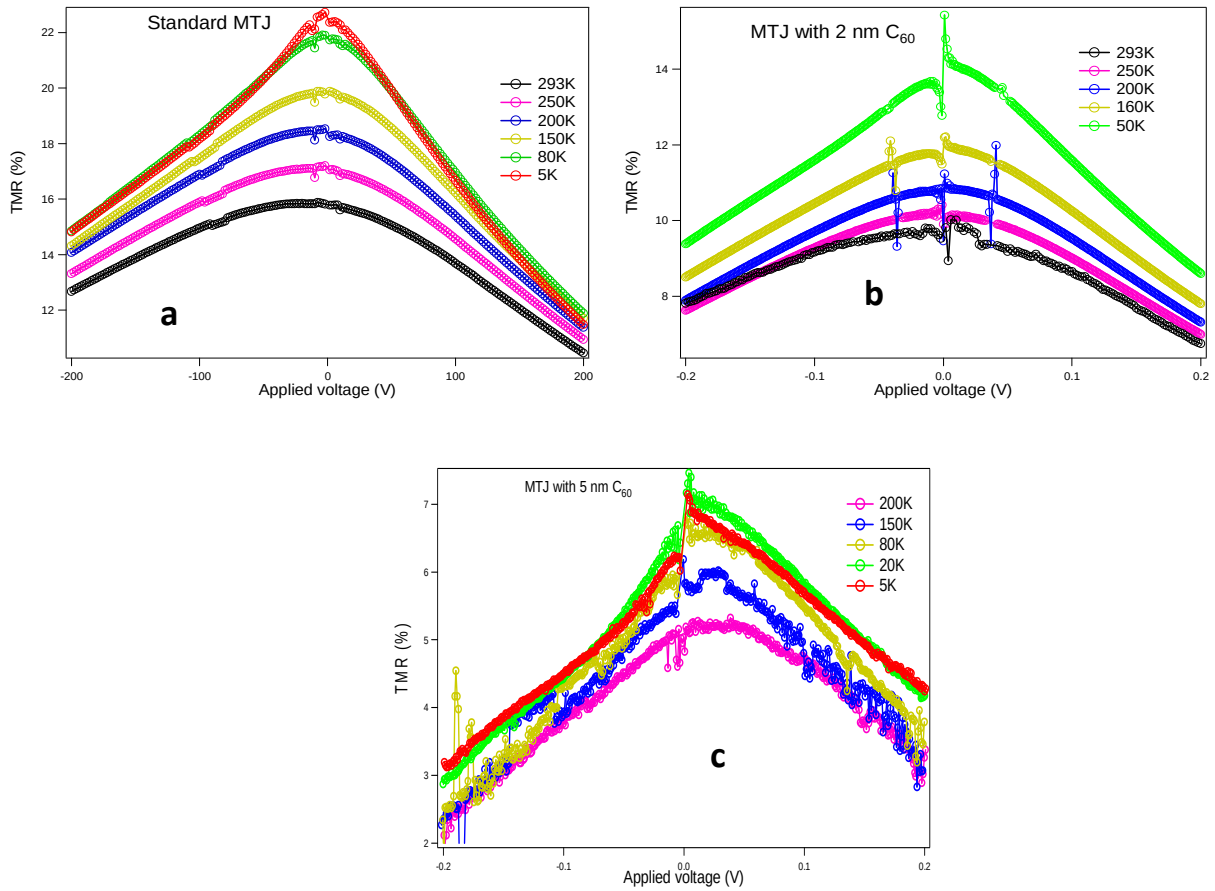

Figure 5.11: TMR(V) curves of (a) standard MTJ, MTJs with (b) 2 nm C_{60} and (c) 5 nm C_{60} measured upon cooling temperature from 293K down to 5K.

Moreover, according to the two-step tunneling model (also discussed in chapter 3), electrons from localized defect states can be activated thermally and these states will create available states for two-step tunneling. Thus, the significant temperature-dependent behavior of the hybrid MTJs may suggest that two-step tunneling dominates the transport mechanism. In summary, my MTJs with thicker C_{60} layers showed, upon reducing the temperature, a strong increase of (1) the TMR, (2) the junction resistance, (3) the non-linearity of the I-V curves, and (4) the bias-dependence of the conductance curves. This behavior confirms tunneling transport through double a barrier and rules out the possibility that metallic charge transport via pin holes

may dominant. Furthermore, based on this behavior, we can identify direct- and multi-step tunneling transport in MTJs with different C_{60} thickness.

MTJs with 10 and 20 nm C_{60} were also fabricated. They show very high resistance and no tunnel magnetoresistive effect at room temperature. These devices were very sensitive to temperature changes and easily became shorted when the temperature was reduced. Thus, it is difficult to interpret the transport mechanism in these devices. However, we obtained extremely non-linear and asymmetric I-V curves at room temperature (Figure 5.12). This behavior suggests that bulk hopping transport via a relatively large amount of intermediate states dominates. The tunneling probability drops exponentially with thickness, so tunneling via an increasing amount of intermediate states will occur as the thickness is increased.

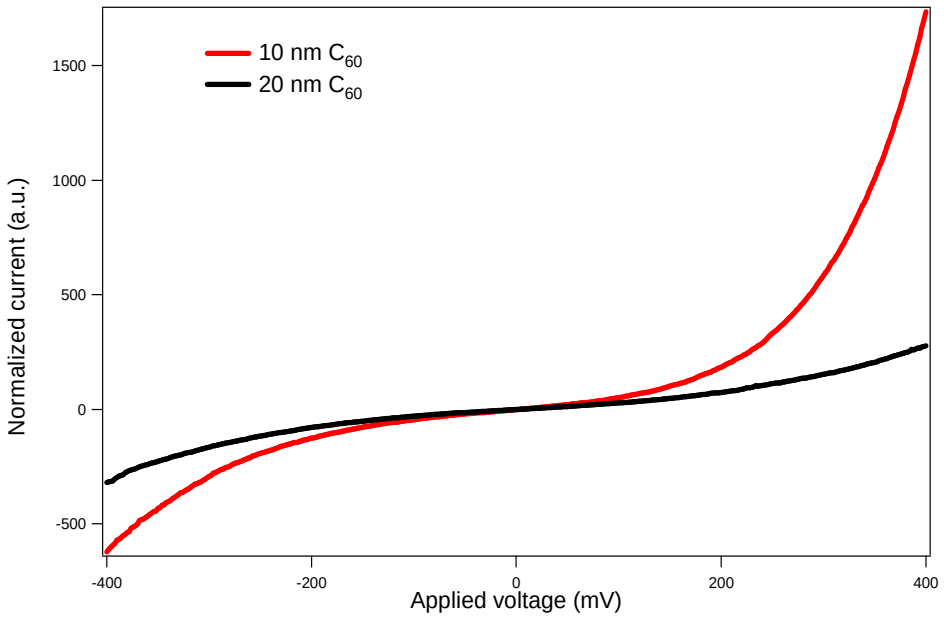

Figure 5.12: Normalized I-V curves of MTJs with 10 and 20 nm C_{60}. These curves were normalized by dividing by their value at near zero bias.

CHAPTER 6

CONCLUSION AND FUTURE OUTLOOK

To summarize, magneto-transport properties of MTJs with the insertion of 1 to 20 monolayers of C_{60} were observed at various temperatures. Their characteristics are also discussed based on current – voltage, conductance – voltage, bias dependence and temperature dependence of the TMR and the junction resistance obtained from measurements. The junction resistance dramatically increases and the TMR decreases with the thickness increase of the C_{60} layer. MTJs with 0–7 nm C_{60} show robust spin-polarized tunneling characteristics, which changes with temperature and applied voltage mostly according to expectation. Moreover, I also qualitatively interpreted and explained the magneto-transport properties of MTJs comprising C_{60} as a function of C_{60} thickness, temperature ad bias voltage. Additionally, we can identify a transition between different transport mechanisms, namely direct- and two-step tunneling, in MTJs with 0–7 nm C_{60}.

Since C_{60} is expected to have extremely long spin life time, the ultimate long-term target of studying spin transport in C_{60} is to develop C_{60}-based spintronic devices as, for example, spin transistors. However, there are many challenges that we need to overcome to achieve that target. An important problem is conductivity mismatch. C_{60} has a very large resistivity which is the main obstacle for efficient spin injection. In the short term, this problem might be solved by doping to reduce the resistance of pure C_{60} and hence overcome the conductivity mismatch problem at the interface of metal/C_{60}. Doping can significantly improve the performance of devices with organic layers such as better carrier injection, more efficient carrier transport and thus lower operation applied voltages. Furthermore, to separate true spin-valve signal from

spurious effects, we can also set-up experiments for measuring spin accumulation using non-local measurements, or electrical Hanle effects.

The study of organic spintronics is still in its early development and requires lots of effort to the fundamental principles of the spin injection, transport and relaxation. More theoretical and experimental work is needed to understand the spin transport mechanism as well as the spin relaxation mechanisms in organic materials. Also, more alternative approaches are required to investigate the role of metal/organic semiconductor interface in the future.

BIBLIOGRAPHY

1. Julliere, M., *Tunneling between Ferromagnetic-Films.* Physics Letters A, 1975. **54**(3): p. 225-226.

2. Moodera, J.S., et al., *Large Magnetoresistance at Room-Temperature in Ferromagnetic Thin-Film Tunnel-Junctions.* Physical Review Letters, 1995. **74**(16): p. 3273-3276.

3. Miyazaki, T. and N. Tezuka, *Giant Magnetic Tunneling Effect in Fe/Al2o3/Fe Junction.* Journal of Magnetism and Magnetic Materials, 1995. **139**(3): p. L231-L234.

4. Sanvito, S., *Organic electronics - Memoirs of a spin.* Nature Nanotechnology, 2007. **2**(4): p. 204-206.

5. Dediu, V.A., et al., *Spin routes in organic semiconductors.* Nature Materials, 2009. **8**(9): p. 707-716.

6. Dediu, V., et al., *Room temperature spin polarized injection in organic semiconductor.* Solid State Communications, 2002. **122**(3-4): p. 181-184.

7. Xiong, Z.H., et al., *Giant magnetoresistance in organic spin-valves.* Nature, 2004. **427**(6977): p. 821-824.

8. Santos, T.S., et al., *Room-temperature tunnel magnetoresistance and spin-polarized tunneling through an organic semiconductor barrier.* Physical Review Letters, 2007. **98**(1): p. -.

9. Barraud, C., et al., *Unravelling the role of the interface for spin injection into organic semiconductors.* Nature Physics, 2010. **6**(8): p. 615-620.

10. Jiang, J.S., J.E. Pearson, and S.D. Bader, *Absence of spin transport in the organic semiconductor Alq(3).* Physical Review B, 2008. **77**(3): p. -.

11. Lin, R., et al., *Distinguishing between tunneling and injection regimes of ferromagnet/organic semiconductor/ferromagnet junctions.* Physical Review B, 2010. **81**(19): p. -.

12. Jansen, R. and J.S. Moodera, *Magnetoresistance in doped magnetic tunnel junctions: Effect of spin scattering and impurity-assisted transport.* Physical Review B, 2000. **61**(13): p. 9047-9050.

13. Moodera, J.S., J. Nowak, and R.J.M. van de Veerdonk, *Interface magnetism and spin wave scattering in ferromagnet-insulator-ferromagnet tunnel junctions.* Physical Review Letters, 1998. **80**(13): p. 2941-2944.

14. E, P.M.a.S.C., *Electronic Processes in Organic Crystals and Polymers*. 2nd ed. 1999: Oxford University Press.

15. Johnson, M. and R.H. Silsbee, *Interfacial Charge-Spin Coupling - Injection and Detection of Spin Magnetization in Metals.* Physical Review Letters, 1985. **55**(17): p. 1790-1793.

16. Fabian, J. and S. Das Sarma, *Spin relaxation of conduction electrons.* Journal of Vacuum Science & Technology B, 1999. **17**(4): p. 1708-1715.

17. Bobbert, P.A., et al., *Spin relaxation and magnetoresistance in disordered organic semiconductors.* Synthetic Metals, 2010. **160**(3-4): p. 223-229.

18. Prigodin, V.N., et al., *Anomalous room temperature magnetoresistance in organic semiconductors.* Synthetic Metals, 2006. **156**(9-10): p. 757-761.

19. J. D. Bergeson, V.N.P., D. M. Lincoln, and A. J. Epstein, *Inversion of Magnetoresistance in Organic Semiconductors.* PHYSICAL REVIEW LETTERS, 2008. **100**.

20. Elliott, R.J., *Theory of the Effect of Spin-Orbit Coupling on Magnetic Resonance in Some Semiconductors.* Physical Review, 1954. **96**(2): p. 266-279.

21. Dyakonov, M.I. and V.I. Perel, *Spin Relaxation of Conduction Electrons in Noncentrosymmetric Semiconductors.* Soviet Physics Solid State,Ussr, 1972. **13**(12): p. 3023-3026.

22. Fabian, J., et al., *Semiconductor spintronics.* Acta Physica Slovaca, 2007. **57**(4-5): p. 565-907.

23. CAMPBELL, A.F.a.I.A., *Transport properties of ferromagnetic transition metals.* J. Phys. Colloques, 1971. **32**: p. C1-46-C1-50.

24. Mott, N.F., *Electrons in Transition Metals.* Advances in Physics, 1964. **13**(51): p. 325-422.

25. P. C. van Son, H.v.K., and P. Wyder, *Boundary Resistance of the Ferromagnetic-Nonferromagnetic Metal Interface.* Physical Review Letters, 1987. **58**: p. 2271–2273.

26. G. Schmidt, D.F., and L. W. Molenkamp, *Fundamental obstacle for electrical spin injection from a ferromagnetic metal into a diffusive semiconductor.* Physical Review B, 2000. **62**.

27. Rashba, E.I., *Theory of electrical spin injection: Tunnel contacts as a solution of the conductivity mismatch problem.* Physical Review B, 2000. **62**(24): p. R16267-R16270.

28. Smith, D.L. and R.N. Silver, *Electrical spin injection into semiconductors.* Physical Review B, 2001. **64**(4).

29. Slonczewski, J.C., *Conductance and exchange coupling of two ferromagnets separated by a tunneling barrier.* Phys Rev B, 1989. **39**.

30. Zhang, S., et al., *Quenching of magnetoresistance by hot electrons in magnetic tunnel junctions.* Physical Review Letters, 1997. **79**(19): p. 3744-3747.

31. White, J.Z.a.R.M., *Voltage dependence of magnetoresistance in spin dependent tunneling junctions.* J. Appl. Phys., 1998. **83**.

32. Shang, C.H., et al., *Temperature dependence of magnetoresistance and surface magnetization in ferromagnetic tunnel, junctions.* Physical Review B, 1998. **58**(6): p. R2917-R2920.

33. Vedyayev, A., et al., *Resonant spin-dependent tunneling in spin-valve junctions in the presence of paramagnetic impurities.* Physical Review B, 2001. **6305**(6): p. -.

34. T. Zijlstra, C.F.J.L., N. Vercruyssen, F. D. Tichelaar, D. N. Loudkov, and T. M. Klapwijk, *Epitaxial aluminum nitride tunnel barriers grown by nitridation with a plasma source.* Appl. Phys. Lett., 2007. **91**.

35. Yuasa, S., et al., *Giant room-temperature magnetoresistance in single-crystal Fe/MgO/Fe magnetic tunnel junctions.* Nature Materials, 2004. **3**(12): p. 868-871.

36. Wang, W.H., et al., *Giant tunneling magnetoresistance up to 330% at room temperature in sputter deposited Co2FeAl/MgO/CoFe magnetic tunnel junctions.* Applied Physics Letters, 2009. **95**(18): p. -.

37. Ikeda, S., et al., *A perpendicular-anisotropy CoFeB-MgO magnetic tunnel junction.* Nature Materials, 2010. **9**(9): p. 721-724.

38. Mitchell, B.S., *An Introduction to Materials Engineering and Science: For Chemical and Materials Engineers*. 2004, John Wiley & Sons, Inc.

39. H. W. KROTO, J.R.H., S. C. O'BRIEN, R. F. CURL & R. E. SMALLEY, *C60: Buckminsterfullerene.* Nature, 1985. **318**: p. 162 - 163.

40. Kratschmer, W., *Fullerenes and fullerites: New forms of carbon.* Nanostructured Materials, 1995. **6**(1-4): p. 65-72.

41. Braun, S., W.R. Salaneck, and M. Fahlman, *Energy-Level Alignment at Organic/Metal and Organic/Organic Interfaces.* Advanced Materials, 2009. **21**(14-15): p. 1450-1472.

42. Kremer, R.K., *High-Temperature Conductivity Study on Single-Crystal C60.* Appl. Phys. A, 1993. **56**.

43. Abrefah, J., et al., *Vapor-Pressure of Buckminsterfullerene.* Applied Physics Letters, 1992. **60**(11): p. 1313-1314.

44. Mort, J., et al., *Electrical-Conductivity Studies of Undoped Solid Films of C60/70.* Chemical Physics Letters, 1991. **186**(2-3): p. 284-286.

45. L.Firlej, A.Z.a., *Resistivity in C60 thin films of high crystallinity.* Solid State Communications, Vol. 87, No. 10, pp. , , 1993. **87**(10): p. 893-897.

46. T.D. Nguyen, Y.S., M. Wohlgenannt, T.D. Anthopoulos, *On the role of hydrogen in organic magnetoresistance: A study of C60 devices.* Synthetic Metals, 2007. **157**: p. 930 – 934.

47. Arthur, J.R., *Molecular beam epitaxy.* Surface Science, 2002. **500**(1-3): p. 189-217.

48. Gobbi, M., et al., *Room-temperature spin transport in C60-based spin valves.* Adv Mater, 2011. **23**(14): p. 1609-13.

49. Cuniberti, G.F., Giorgos; Richter, Klaus, *Introducing Molecular Electronics*. 2005, Springer, Berlin Heidelberg.

50. Schoonus, J.J.H.M., et al., *Magnetoresistance in Hybrid Organic Spin Valves at the Onset of Multiple-Step Tunneling.* Physical Review Letters, 2009. **103**(14): p. -.

51. W. F. Brinkman, R.C.D., and J. M. Rowell, *Tunnel Conductance of Asymmetrical barriers.* J. Appl. Phys., 1970. **41**(5).

52. S. P. Dash, S.S., J. C. Le Breton, H. Jaffrès, J. Peiro, J. -M. George, A. Lemaître, R. Jansen, *Spin precession and decoherence near an interface with a ferromagnet.* arXiv:1101.1691, 2011.

53. Poplavskyy, D. and J. Nelson, *Nondispersive hole transport in amorphous films of methoxy-spirofluorene-arylamine organic compound.* Journal of Applied Physics, 2003. **93**(1): p. 341-346.